AFRL-RV-PS-
TR-2012-0055

AFRL-RV-PS-
TR-2012-0055

CONSTRUCTING A CLIMATOLOGY OF WHISTLER WAVE ENERGY FROM LIGHTNING IN LOW EARTH ORBIT

Jonah J. Colman

December 16, 2011

Interim Report

AIR FORCE RESEARCH LABORATORY
Space Vehicles Directorate
3550 Aberdeen Ave SE
AIR FORCE MATERIEL COMMAND
KIRTLAND AIR FORCE BASE, NM 87117-5776

DTIC COPY

NOTICE AND SIGNATURE PAGE

AFRL-RV-PS-TR-2012-0055 HAS BEEN REVIEWED AND IS APPROVED FOR PUBLICATION IN ACCORDANCE WITH ASSIGNED DISTRIBUTION STATEMENT.

//signed//	//signed//
Christopher Sillence	Joel B. Mozer
Project Manager, RVBXT	Chief, AFRL/RVB

REPORT DOCUMENTATION PAGE

Form Approved
OMB No. 0704-0188

1. REPORT DATE *(DD-MM-YYYY)*	2. REPORT TYPE	3. DATES COVERED *(From - To)*
16-12-2011	Interim Report	1 Oct 2010 to 1 Oct 2011

4. TITLE AND SUBTITLE
CONSTRUCTING A CLIMATOLOGY OF WHISTLER WAVE ENERGY FROM LIGHTNING IN LOW EARTH ORBIT

5a. CONTRACT NUMBER

5b. GRANT NUMBER

5c. PROGRAM ELEMENT NUMBER
62601F

6. AUTHOR(S)
Jonah J. Colman

5d. PROJECT NUMBER
1010

5e. TASK NUMBER

5f. WORK UNIT NUMBER
299288

7. PERFORMING ORGANIZATION NAME(S) AND ADDRESS(ES)
Air Force Research Laboratory
Space Vehicles Directorate
3550 Aberdeen Ave SE
Kirtland AFB, NM 87117-5776

8. PERFORMING ORGANIZATION REPORT NUMBER
AFRL-RV-PS-TR-2012-0055

9. SPONSORING / MONITORING AGENCY NAME(S) AND ADDRESS(ES)

10. SPONSOR/MONITOR'S ACRONYM(S)
AFRL/RVBXT

11. SPONSOR/MONITOR'S REPORT NUMBER(S)

12. DISTRIBUTION / AVAILABILITY STATEMENT
Approved for public release; distribution is unlimited. (377ABW-2011-1487 dtd 19 Oct 2011)

13. SUPPLEMENTARY NOTES

14. ABSTRACT
Starting from OTD/LIS lightning data representing 1995 – 2005, a climatology is constructed with 1°x1° latitude-longitude spatial resolution, averaged into 2 hour bins for each month of the year. Assuming a linear relationship between optical flash rate and VLF power flux, and that the VLF amplitude drops off as one over distance, a proxy for VLF power is developed. A typical lightning spectrum is then applied and the values are scaled by an appropriate transionospheric absorption for each time and place. These values are mapped up the geomagnetic field lines to low earth orbit altitudes and over to conjugate locations in order to compare them to E-field spectral densities measured by the DEMETER satellite between 2005 and 2009. An overview of the DEMETER survey mode data is presented which leads to a best scaling of the lightning VLF climatology. The final distribution's spatial and temporal variations are compared with the DEMETER data and some implications are discussed.

15. SUBJECT TERMS
VLF, Lightning, Radiation Belts

16. SECURITY CLASSIFICATION OF:			17. LIMITATION OF ABSTRACT	18. NUMBER OF PAGES	19a. NAME OF RESPONSIBLE PERSON
a. REPORT	b. ABSTRACT	c. THIS PAGE			Christopher Sillence
UNCLASSIFIED	UNCLASSIFIED	UNCLASSIFIED	UNLIMITED	48	19b. TELEPHONE NUMBER

This page is intentionally left blank.

Table of Contents

1. SUMMARY 1
2. INTRODUCTION 1
3. METHODS, ASSUMPTIONS, AND PROCEDURES 4
2.1 Organizational Framework 4
2.2 Wave Data 5
2.3 Optical Lightning Data 10
2.4 Interpreting the Wave Data 12
2.5 VLF from Lightning in the Earth-Ionosphere Waveguide 18
2.6 Transionospheric Attenuation 22
2.7 Magnetospheric Propagation 25
2.8 Scaling the Model to DEMETER Observations 27
4. DISCUSSION 29
5. CONCLUSIONS 32
5.1 Terrestrial VLF Source Model 33
5.2 Earth-Ionosphere Waveguide Propagation Model 33
5.3 Trans-Ionospheric Attenuation Model 34
5.4 Magnetospheric Propagation Model 34
REFERENCES 37

List of Figures

1. Organizational Framework 4
2. Coordinate Systems 5
3. Histograms of Contributing Observations from DEMETER....6
4. Representative VLF Spectral Densities from DEMETER Averages 7
5. Representative Histograms of VLF Spectral Densities from DEMETER Averages....8
6. Representative Annual Histograms of VLF Spectral Densities from DEMETER 10
7. Temporal Optical Flash Climatology....11
8. Representative Spatial Optical Flash Climatology 12
9. DEMETER Spectral Density vs. Frequency....13
10. DEMETER Spectral Density, Frequency vs. Longitude 14
11. Hemispheric July Spectral Densities, Frequency vs. Longitude....16
12. Hemispheric January Spectral Densities, Frequency vs. Longitude....17
13. Representative Spatial Pseudopower Climatology 21
14. Transionospheric Absorption, Representative Spatial Climatology....23
15. Pseudopower in Low Earth Orbit, Representative Spatial Climatology....24
16. Pseudopower Climatology in Low Earth Orbit, Magnetospheric Propagation 26
17. Climatology Scaling Factors and Correlation Coefficients 28
18. Spatial Plots of the Scaled Climatology and DEMETER Averages....30
19. Spectral Density of the Scaled Climatology vs. Apex Radius....32

List of Tables

1. Frequency Averaged Scaling Factors 29

1. SUMMARY

Knowledge of the intensity of electromagnetic radiation in the radiation belts is a key component to understanding the lifetimes and overall behavior of the energetic particles existing there. These particles can damage spacecraft as well as human tissue exposed to them. Very Low Frequency (VLF) radiation from lightning is thought to be an important contributor to this interaction. Here we attempt to construct a climatology of VLF wave energy from lightning in low earth orbit, which can be used to estimate its intensity throughout the radiation belt region. The final distribution's spatial and temporal variations are compared with the in situ data and found to capture all of the salient features. This represents the first global climatology of this type and should be used in situations where estimates of the VLF intensity from lightning are a necessary component of a mission or analysis.

2. INTRODUCTION

It is important to understand the intensities and origins of VLF radiation in the inner magnetosphere primarily in order to characterize the sources and sinks of energetic electrons in the radiation belts. The radiation belts contribute to reducing satellite lifetime in orbit, as well as being a primary hazard to human health during space travel. Precipitating electrons from the radiation belts are thought to affect the chemistry of the middle atmosphere, e.g. [1, 2], and may contribute to the poorly understood sensitivity of the earth's climate to solar variability as exemplified by the Milankovitch cycles. Previous work constructing climatologies of VLF radiation from satellite data have shown their utility in enhancing our understanding of these important sources and sinks, e.g. [3, 4, 5]. Constructing a climatology of VLF from lightning can help us to categorize and separate terrestrial/non-terrestrial and anthropogenic/non-anthropogenic sources and therefore contributions to radiation belt particle lifetimes. In addition, understanding the contribution of lightning to VLF intensity in low earth orbit (LEO) is important in order to help separate and characterize the global propagation characteristics of VLF radiation both within the earth-ionosphere waveguide and through the ionosphere.

The magnetosphere represents the area near the earth whose composition is not immediately dominated by the flow of the solar wind, but is partially shielded by the deflecting effects of the earth's magnetic field. Within the inner magnetosphere the Earth's magnetic field dominates and can be reasonably represented without an external field model. This region generally extends to around 6 Earth radii ($R_E \approx 6372$ km). Lying within the inner magnetosphere are the radiation belts, where the motion of energetic electrons ($\sim$1 keV – 5 MeV) are confined by the earth's magnetic field. The radiation belts are roughly toroidal in shape, following lines of force of the geomagnetic field. The inner and outer radiation belts are separated by a 'slot' region where there are fewer energetic particles. The location of this slot is energy dependent and has provided a test for theories attempting to explain the existence of the radiation belts. The inner radiation belt is relatively stable and transient injections have been observed to occur only during strong geomagnetic storms, e.g. [6, 7]. Energetic electron densities in the outer radiation belt are relatively dynamic and more closely linked to solar activity. The electron slot occurs around L = 2.5 - 3.5 and depends on electron energy in such a way as to suggest that loss rates due to wave-particle interactions are dominant within that region [8]. The inner radial edges of the radiation

belts are regions where the atmospheric neutral density is large enough to make Coulomb interactions the dominant sink for energetic electrons.

VLF radiation plays a central role in the plasma dynamics of the inner magnetosphere. The energetic electron distribution function in the region is generally thought to be controlled by wave particle interactions and Coulomb scattering. Doppler shifted cyclotron resonant interactions between whistler mode plasma-waves (10s of Hz up to 10s of kHz) and energetic electrons in the radiation belts can cause pitch angle scattering in the particles. This can lead to deeper penetration towards the earth along their bounce paths, which leads to enhanced Coulomb scattering. Coulomb scattering causes energy loss which in turn enhances the rate of Coulomb scattering. This process drives a cascade ending in the deposition of all of the energetic electron's energy in the upper atmosphere; a process known as electron precipitation. Wave-particle interactions can also lead to the growth of whistler waves in a process known as amplification due to resonant instability [9]. Despite decades of study it has proven difficult to show conclusively what the dominant source and loss processes are for energetic electrons in various parts of the magnetosphere, in part because of a lack of understanding about the sources and sinks of the waves involved.

Theoretical treatments of energetic electron lifetimes within the radiation belts rely on empirical estimates of the electron distribution functions and lifetimes, but also on estimates of the wave energy thought to exist there. In seminal work by Able and Thorne [10, 11, 12], estimates were made for the wave intensity, occurrence rate, and propagation angle of all waves then thought to contribute to particle lifetimes. These included Plasmaspheric Hiss (estimated from work by Thorne et al., [13]; and Tsurutani, Smith, and Thorne, [14]), Lightning-Generated Whistlers (estimated from Burgess and Inan, [15]; and Draganov et al., [16]), and VLF Transmitter Signals (estimated from Inan, Chang, and Helliwell, [17]). Utilizing bounce-averaged quasi-linear pitch angle diffusion coefficients, the equilibrium distribution functions and precipitation lifetimes calculated were found to accurately describe characteristic structures observed in the radiation belts. This conclusion was recently called into question by a reanalysis of the transmitter signal estimates by Starks et al. [18,19], which suggested that median field strengths were overestimated by roughly 20 dB and so could not impact electron lifetimes as necessitated by the Able and Thorne analysis. Due to the coupled nature of these calculations this suggests that the other assumptions made by Able and Thorne [10] should be revisited.

Lightning generated whistlers (LGW) begin as radio frequency electromagnetic impulses created by the currents in lightning strokes. These impulses are commonly known as sferics. Sferics are converted into plasma waves at the lower ionospheric boundary and from there obey the conventions of a plasma wave in a magnetized cold plasma. That is, the propagating modes are right hand circularly polarized waves below the local electron cyclotron and plasma frequencies, and above the ion cyclotron frequency. They travel along trajectories determined by the local magnetic field and plasma properties (e.g. electron density gradients and positive ion populations). They are known as whistlers because their frequency range overlaps with the audio and they can sometimes be detected by radio receivers on the ground after having traveled through the inner magnetosphere. On this journey they become dispersed in frequency and so 'whistle' characteristically, with higher frequencies arriving first [20].

In order to be observed from a ground station it is thought that whistlers must be guided by a field aligned density irregularity or 'duct'. This is because Ducts constrain the motion and wave normal of the VLF radiation to be along the field line, and the propagation angle with respect to the external magnetic field near a strong gradient in refractive index (like the top or bottom of the ionosphere) must be near zero or reflection will occur. Non-ducted waves become oblique over time, that is their wave normal becomes transverse to the local magnetic field, so they do not penetrate the ionosphere. Non-ducted VLF radiation undergoes spectral dispersion in space as well as time, as the guiding effect of the magnetic field is frequency dependent. Many non-ducted whistler trajectories include frequency dependent inversions to their group velocity direction with respect to the geomagnetic field known as magnetospheric reflections. These are distinct from reflections occurring at strong gradients in the refractive index and rely on the closing of the refractive index surface for a wave with frequency near the local lower hybrid surface [21]. Whistlers that undergo these events are known as magnetospherically reflected (MR) whistlers. A given whistler may undergo a number of reflections before dropping below detectability.

Whistlers are often characterized based on how many reflections they have experienced. A whistler heading directly up through the ionosphere to a satellite location is called a 0+, or fractional hop, whistler and one headed down at a satellite (or ground station) after passing the magnetic equator once being called a 1- (or single hop) whistler. Both ducted and nonducted whistlers have been observed in the magnetosphere [22] but space based observations of ducted whistlers are rare. The fact that multi-hop whistlers can be observed from the ground testifies to the stability of some field aligned ducts. The issue of what fraction of whistler energy is ducted is central to calculating their importance to radiation belt electron lifetimes. This is because the phase direction of ducted whistlers remains field aligned, while that of non-ducted whistlers becomes oblique with respect to the local geomagnetic field and though their group velocity is guided by the field direction they do not follow it closely. Oblique whistlers are individually less efficient at producing the pitch angle scattering which results in electron precipitation [23], but these may be more numerous or have a small effect in a wider range of situations [24]. The relative prevalence and climatology of ducts in the plasmasphere and inner magnetosphere is still an active area of research.

Lightning-induced electron precipitation (LEP) events associated with whistlers have long been detected from rockets [25], satellites [26], and from the ground [27]. Observing correlations between satellite based measurements of precipitating electrons and ducted whistler observations at Palmer Station, Antarctica, Voss et al. [28] suggested that detectable LEP events are driven primarily by ducted whistlers, supporting previous work by Burgess and Inan [15] which analyzed only ground based observations. Lauben, Inan, and Bell [24] and later Bortnik, Inan, and Bell [29] focused on nonducted whistler wave energy and concluded that it may play a role in the formation and maintenance of the slot region. Inan et al. [30] interpreted satellite data on precipitating electron flux timing, number, and energy in the context of a nonducted interaction model and showed reasonable agreement. That work also observed large regions associated with thunderstorms containing enhanced precipitating electron flux, and suggested that they are produced and maintained by lightning. These regions showed up as large scale enhancements to the overall background electron density, and not discrete impulsive events. These observations emphasize that it is important to understand the overall climatology of LGW and how they

couple into, and are transported within, the magnetosphere; as well as from the perspective of individual LEP events. This broader perspective was also shown to be useful in work by Gemelos et al. [31], which demonstrated a seasonality in electron precipitation consistent with lightning and inferred that lightning is a significant contributor to the formation of the slot region.

Using satellite observations to infer that specific precipitation events are driven by specific observed whistlers has proven difficult because sferics in the earth ionosphere waveguide can generate whistlers out to at least 1000 km [32,33], and even that appears to be an observational rather than theoretical limit. Sferics are routinely observed on the ground at distances of 6000 km [34] or more from their originating lightning strike depending on the frequency range investigated [35]. It similarly becomes more difficult to positively identify a sferic observed on the ground with a whistler observed in orbit as the distance between the observations grows. Propagation of the sferics within the earth ionosphere waveguide is nonuniform, as is transionospheric absorption. Additional low altitude and/or columnar ionization drives additional adsorption; situations favored during the daytime and at low latitudes. It also seems that there are locations where the transformation from a sferic to a whistler is more or less efficient such that observation at certain locations is more likely, e.g. [36]. A final complication occurs because the electromagnetic pulse generated by a lightning strike can actually modify the ionosphere as it passes, generating optical emissions such as 'elves', causing local heating of electrons, and even driving ionization which in turn changes the local refractive index.

3. METHODS, ASSUMPTIONS, AND PROCEDURES

2.1 Organizational Framework

The intent of this study is to construct a climatology of whistler wave energy from lightning at 660 km. The approach followed here is to start from previously constructed climatologies of lightning near the earth's surface. That distribution is then considered as a source of VLF energy, which can propagate within the earth-ionosphere waveguide. The VLF energy in the waveguide can then leak out and undergo trans-ionospheric attenuation, the most important portion of which occurs below 660 km. In order to properly validate the resulting power distribution with satellite measurements, propagation within the magnetosphere must also be considered; including potentially the effects of the plasmasphere and plasmapause. A schematic for this approach is shown in Figure 1.

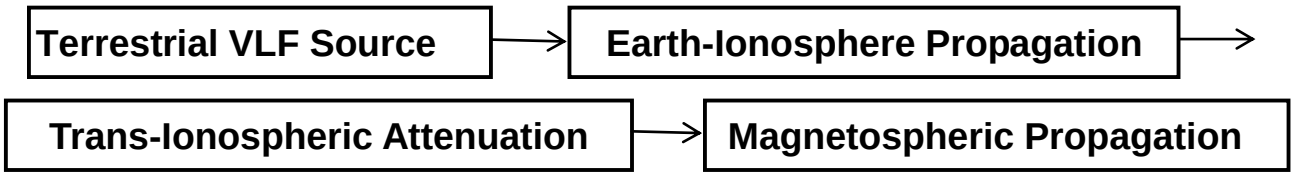

Figure 1. Organizational Framework

A number of different levels of fidelity are possible for each step in this procedure, and options for each of these will be discussed in turn. Ideally the resulting climatology would be a function

of frequency, local time, day of year, spatial location, as well as some measure of solar activity, and would specify both the Poynting and wave normal vectors. We will attempt to meet these requirements while being constrained by available observational and computational resources. In this initial study the model will be scaled to measurements of VLF E-field spectral density taken by the DEMETER satellite.

Some discussion of the coordinate systems employed here is also warranted. Wave data typically organizes around magnetic rather than geographic latitudes, and both systems will be used here. For magnetic coordinates an apex system is employed [37], these follow field lines and consist of the apex radius (or apex latitude), apex longitude, and height above geoid (which specifies two points on the field line one for the northern and one for the southern hemisphere). Field line apexes were calculated using IGRF11 and a simple field line tracer employing a fourth order Runga-Kutta stepping algorithm with a curvature dependent step size. One advantage of the apex coordinate for our purposes is that a given apex corresponds to a specific field line and so map directly to the conjugate point, though there may be a longitudinal shift involved. Two categorizations of the apex coordinate will be utilized here: the apex radius normalized to the earth's radius, $A = 1 + (h_A/R_E)$, where h_A is the maximum height (apex) of the field line above the geoid, and R_E is the radius of the earth; and the apex latitude, $\lambda_A = \pm\cos^{-1}(1/\sqrt{A})$. Figure 2a shows contours of constant apex latitude overlaid on a world map, while Figure 2b compares the apex radius at a height of 700 km with the McIlwain L shell [38] at the same height. Figure 2b shows the close correspondence between the Apex Radius and the McIlwain L, with average contour values being the same but with the McIlwain L going to higher values where the geomagnetic field is relatively weak (near the south Atlantic anomaly) and to lower values where the geomagnetic field is relatively strong, in order to keep the longitudinal invariant constant, $I = \oint_A^{A'} (1 - B_l/B)^{1/2} ds$[38].

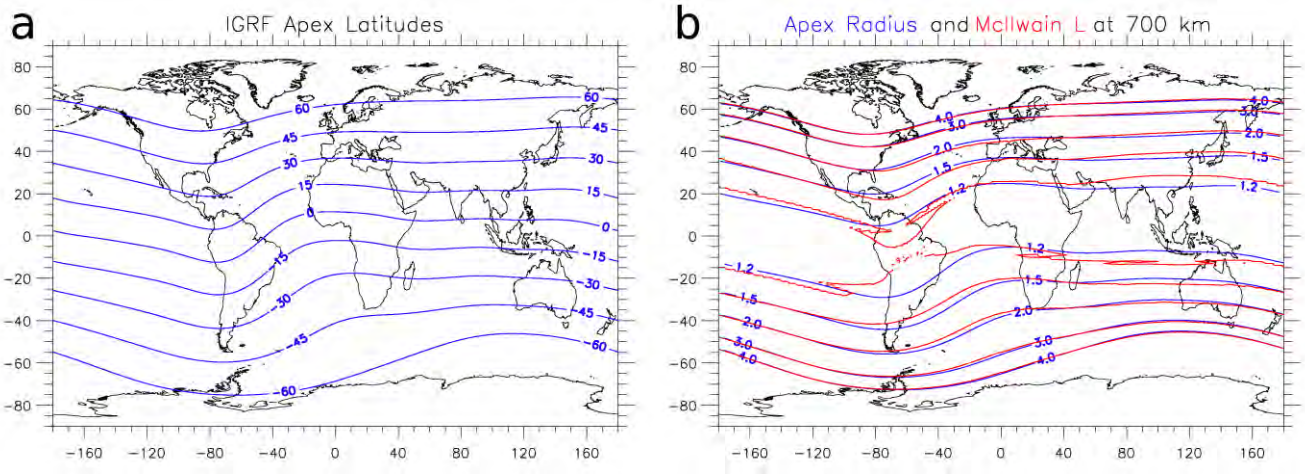

Figure 2. Coordinate Systems

2.2 Wave Data

The wave data used in this study were obtained from the Instrument Champ Electrique experiment [39] aboard the French micro-satellite DEMETER. Originally launched in June 2004

at an orbit altitude of 710 km, it was lowered to 660 km in December 2005. Here we analyze electric field spectral amplitudes in the ELF/VLF range, from 10 Hz up to 20 kHz at a resolution of 19.53125 Hz, collected between January 2005 and December 2009. The stated sensitivity and dynamic range in the VLF are 0.05 μV/m/√Hz and >80 dB respectively, with an instrumental noise of 0.03 – 0.05 μV/m/√Hz. Only survey mode data is used here where the electric field component is perpendicular to the orbital plane (sensor component: E12). DEMETER's orbit is quasi-sun-synchronous and so measurement times are centered on two local times, around 1030 and 2230 for downward and upward orbits respectively. Data at latitudes above about 65˚ were not collected. We use the "VLF electric spectrum" data type (APID 1132, Type 0), which consist of two consecutive spectra each individually consisting of an on-board average of 40 spectra collected over a duration of 2.048 seconds. This data product is available nearly continuously during the DEMETER mission.

In order to investigate the data in a climatological sense they are averaged into 1˚x1˚ geographic latitude and longitude spatial bins for each half orbit for each month of the year. The data are also averaged over 5 frequency bins to give a final spectral resolution of 97.65625 Hz. The averaging procedure involves summing all spectral densities and recording the number of observations which contribute. The average is then the total spectral density divided by the total number of observations. This same approach was taken when averaging across other dimensions, e.g. when averaging over apex latitudes all spectral densities within the range was summed and then divided by the number of observations to give an average. Although the data is often presented as the log of the spectral density, in no cases were averages performed on the log transformed data.

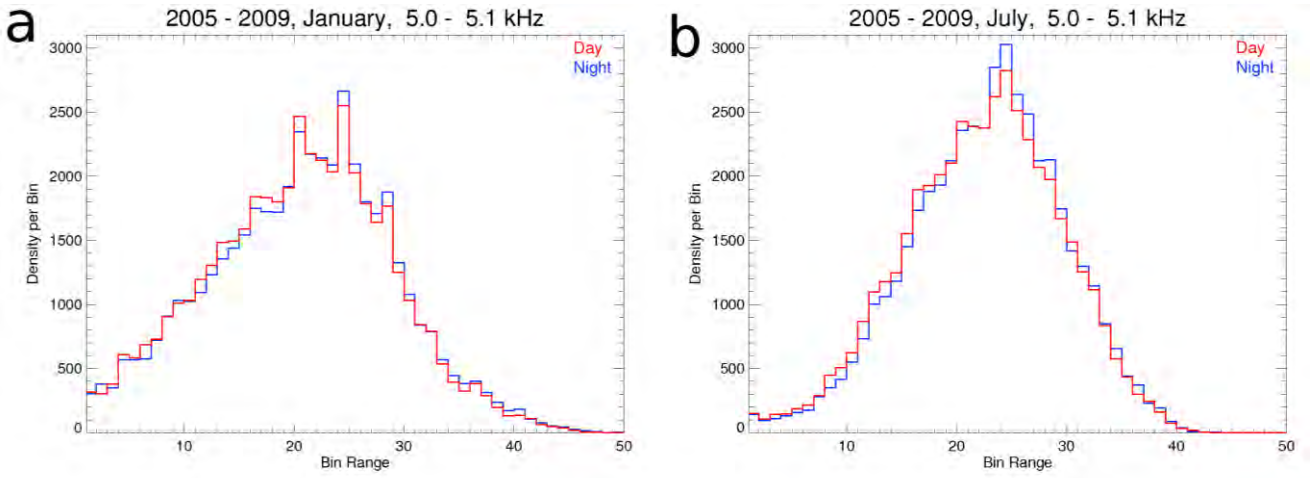

Figure 3. Histograms of Contributing Observations from DEMETER

Figure 3 shows a Histogram of the number of observations contributing to each spatial/temporal average considered here during January and July at 5 kHz. The bulk of the locations have 20 – 30 observations making up their averages (corresponding to 800 – 1200 individual spectra), thus giving us some confidence in their validity as averages and explaining somewhat the binning dimensions employed. Figure 4 shows some representative spatial plots of the data overlaid on a global map of continental outlines, and Figure 5 shows the same data plotted as histograms. Both Figure 4 and 5 show averaged data from all years of DEMETER operation at 5000 – 5078 Hz

separated into upward (nighttime) and downward (daytime) orbits for January and July. Both figures show the data in spectral density units of log($\mu V^2/m^2/Hz$) and the histogram was constructed using a bin size of 0.025 log($\mu V^2/m^2/Hz$).

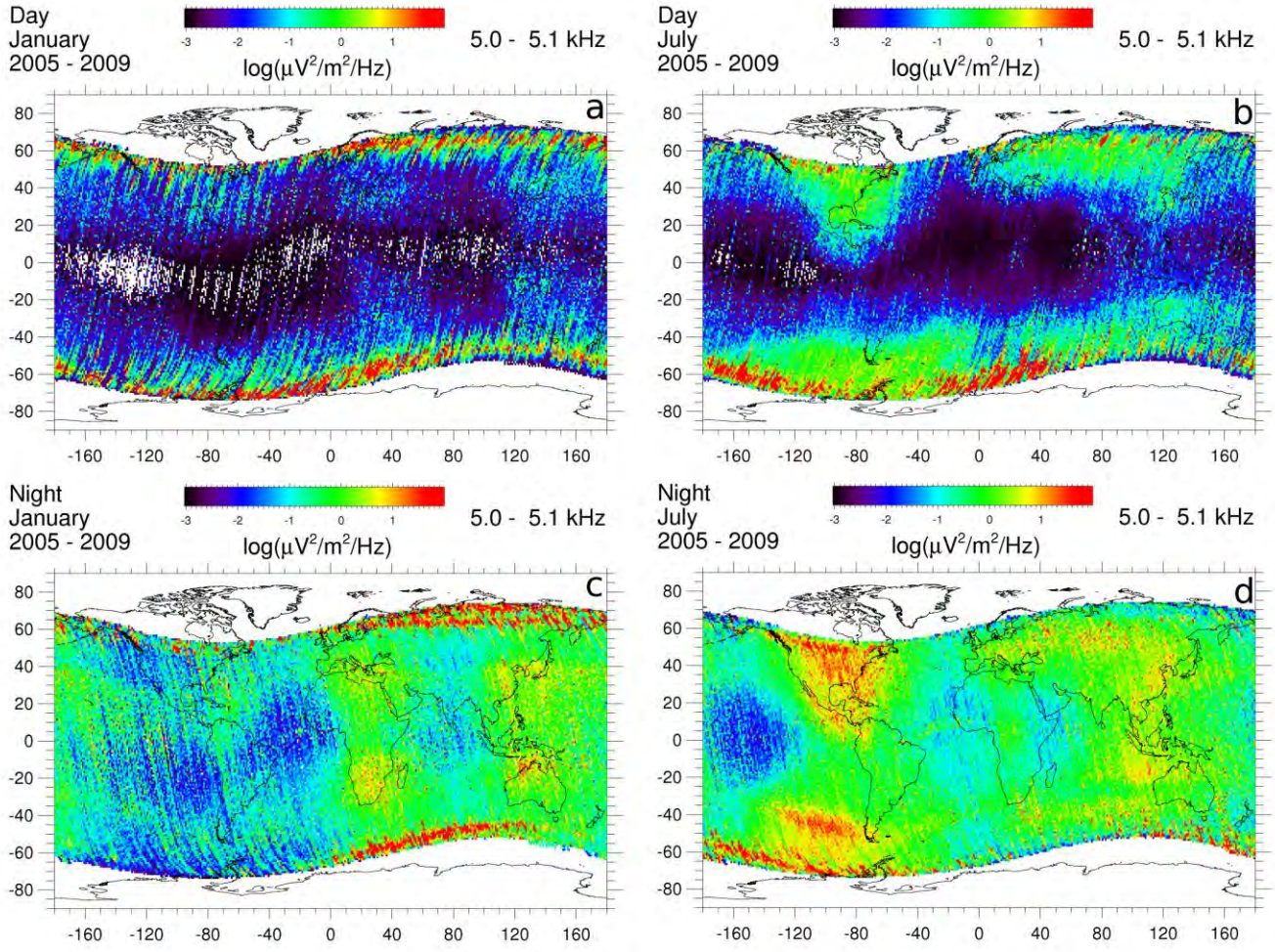

Figure 4. Representative VLF Spectral Densities from DEMETER Averages

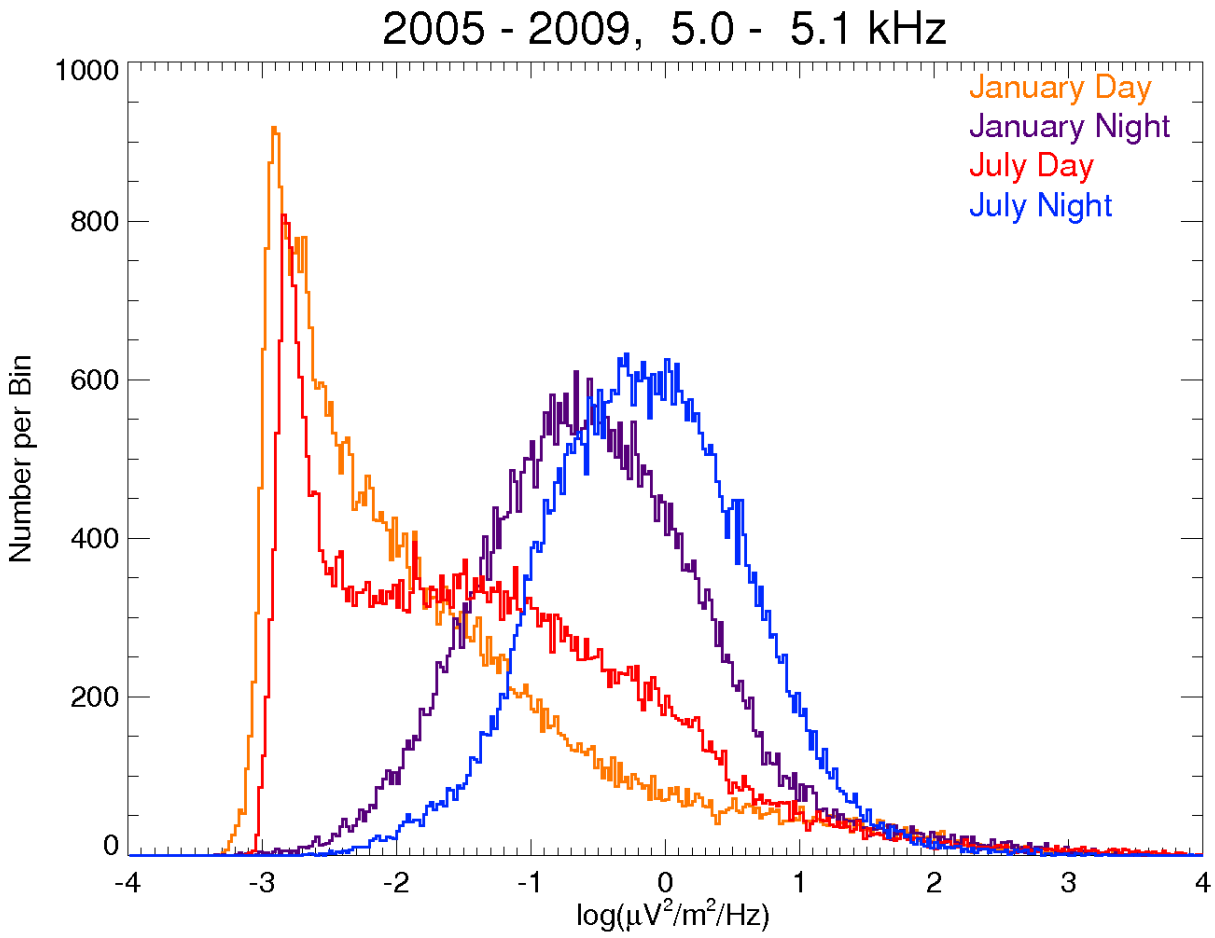

Figure 5. Representative Histograms of VLF Spectral Densities from DEMETER Averages

While the nighttime distributions look smooth and normally distributed (in log(power) space), with the mean value in July being significantly higher than it is in January, it is clear that both sets of daytime spatial averages push up against the instrumental noise floor (~ -2.8 $\log(\mu V^2/m^2/Hz)$ at 5 kHz from Figure 4 in Berthelier et al. [39]) in a significant number of the averaged values. It is also noteworthy that the data does not simply cut off at the sensitivity value, but shows a second distribution as the noise floor is approached. This reflects the fact that each grid average itself contains a distribution of events and each spectrum is itself the on-board average of 40 spectra. This has consequences for the interpretation of the data, e.g. the true range of magnitudes is not represented and unresolved impulsive events are simply time averaged into the resulting values. It also accounts for the relatively wider peak associated with the 'January Day' values near the noise floor as more individual spectra below the cutoff would have been integrated into each survey mode value.

In the case of the July, daytime distribution it appears as if there is a symmetric distribution centered around -1.5 $\log(\mu V^2/m^2/Hz)$, which is superimposed on the noise floor distribution centered around -2.8 $\log(\mu V^2/m^2/Hz)$. It is not clear if a similar symmetric distribution exists in the January, daytime data, if so it is obscured by the noise floor. In fact it is not immediately clear why the entire spatial distribution of log(power) VLF should be normally distributed at all.

This implies that the distribution is created by a series of uncorrelated events whose effects are multiplicative; perhaps the distribution of power from lightning strokes and the absorption due to transionospheric propagation. Their covariance should be small but their contribution to power measured at the satellite is multiplicative (Sferic Power x Transionospheric Absorption $\propto$ Power Received).

It is of note that both Figure 4 and 5 show significant diurnal and seasonal variation. These features along with systematic spatial features will be discussed in later sections. As a check on the year to year uniformity of the data an additional histogram of the July averages at 5 kHz for each year of data individually is presented in Figure 6. The shape of the distribution function is nearly identical within each year with variation mostly in the total number of samples collected, e.g. there were significantly fewer samples archived in 2005, the first full year of the DEMETER mission. There is also a slight preponderance of values above 1 $\mu V^2/m^2/Hz$ in the daytime 2005 values compared with values between 0.01 and 0.1 $\mu V^2/m^2/Hz$, this is most likely due to the more active sun during that period. These emissions belong to class of intense typically broadband emission observed along the auroral oval (as seen in Figure 4) which don't show the seasonality of lightning. It is not expected that the change in altitude from ~700 to ~660 km at the end of 2005 would have a major impact on transionospheric attenuation since the majority of absorption takes place at the lower edge of the ionosphere (60-100 km) where ion-neutral collisions are high, and the remaining part is due to Coulomb interactions integrated along the path [40] which should peak at the F layer. It is likely that these emissions are related to events in the outer magnetosphere which are more easily driven by solar conditions. It is also possible that more active solar conditions would affect amplification of whistler energy during its passage through the inner magnetosphere. In our analysis of lightning we will in general take measures to exclude auroral phenomena.

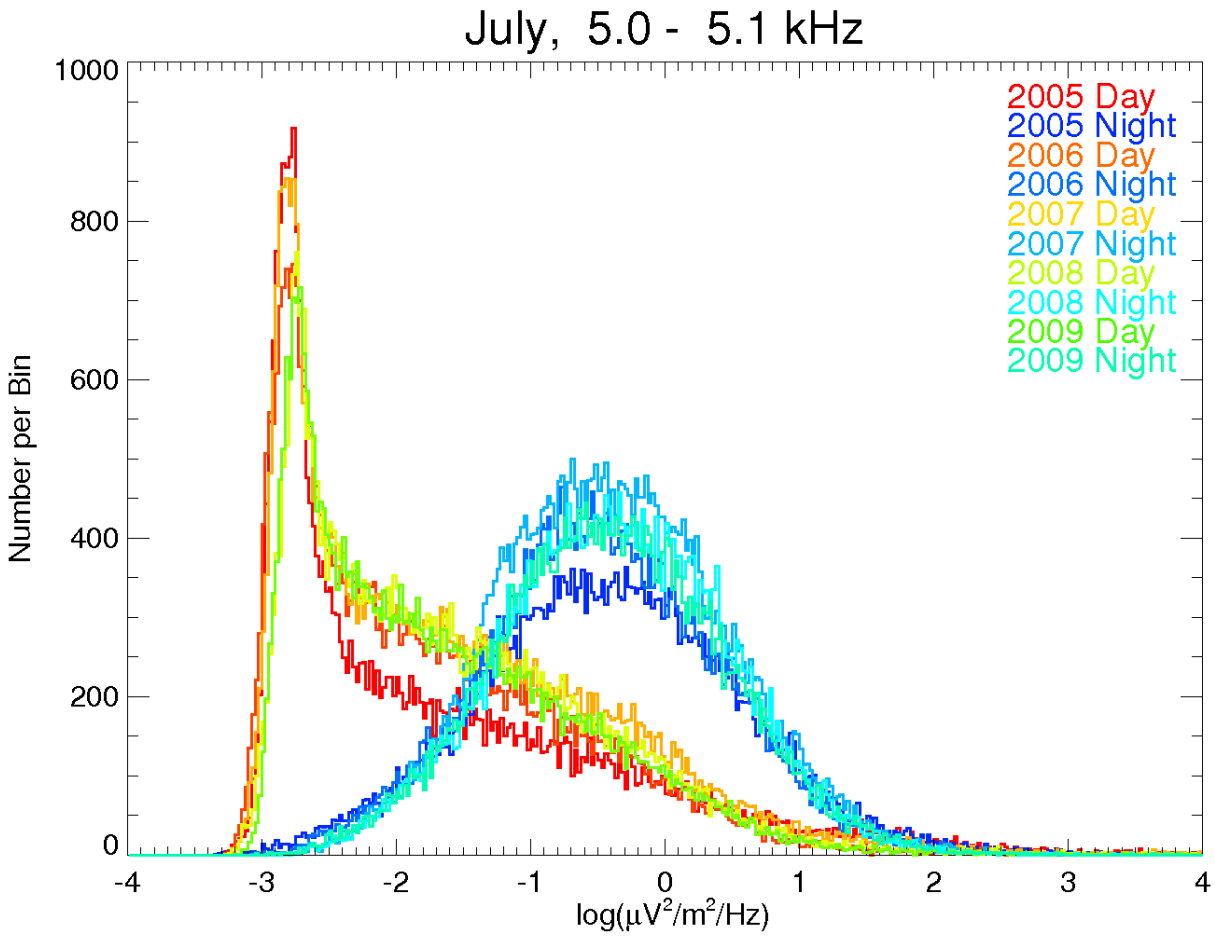

Figure 6. Representative Annual Histograms of VLF Spectral Densities from DEMETER

2.3 Optical Lightning Data

The optical lightning flash data used here were collected by the Optical Transient Detector (OTD) and its successor instrument the Lightning Imaging Sensor (LIS). Inter-calibrated and merged data products were downloaded from a NASA maintained website (http://thunder.msfc.nasa.gov/data/index.html) between October and December 2010. Two different available climatologies were combined for our purposes: the HRMC_COM_FR (monthly), which has a 0.5 degree spatial resolution and monthly temporal resolution; and the LRADC_COM_SMFR2, which has 2.5 degree spatial resolution and 2 hr temporal resolution for every day of the year. From these a combined climatology with 1 degree spatial resolution and an average diurnal cycle (with 2 hr resolution) for each average monthly value were constructed. The averaging procedure involved deresolving the HRMC_COM_FR to 1 degree spatial resolution, then constructing an average diurnal cycle for each month from LRADC_COM_SMFR2 and interpolating that to 1 degree resolution, this was normalized and applied to the deresolved HRMC_COM_FR set. Figure 7a shows the global monthly averages and Figure 7b the global annual average diurnal cycle of the combined climatology. The two vertical lines in Figure 7b represent the average local time of DEMETER overpasses. Both

Figure 7a and 7b show the canonical average of 44±5 lightning flashes occurring around the globe every second [41].

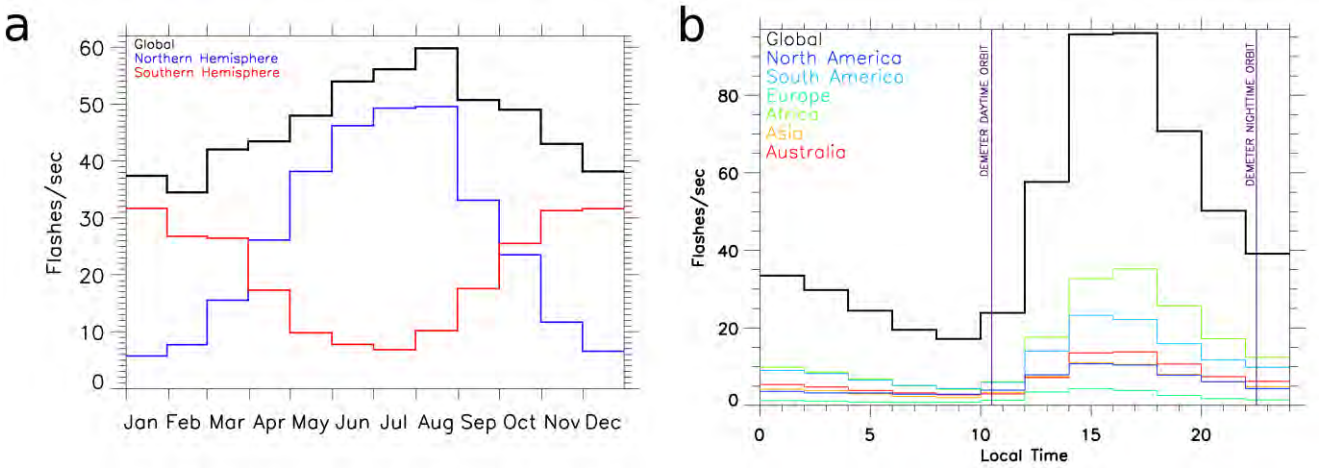

Figure 7. Temporal Optical Flash Climatology

Figure 7a also shows the monthly averages separated into hemispheres (red for the Southern Hemisphere and blue for the Northern Hemisphere), and the dominance of the northern hemisphere on the overall global cycle is clearly evident, this effect is primarily due to the preponderance of land mass in the northern hemisphere. Figure 7b also shows the diurnal cycle broken into the major land mass areas (along with surrounding oceans following the grouping of Lay et al., [42]) as different colored lines (North America in blue, South America in light blue, Europe in green, Africa in light green, Asia in yellow, and Australia in red) and while we see a universality to the shape of the diurnal cycle around the world there are also variations in peak time and relative amplitude. The region to region differences shown here are consistent with those shown at a higher temporal resolution in Mach et al. [43] (also from OTD/LIS data). Mach et al. [43] also present OTD/LIS data limited to oceanic observations. These show a much less pronounced diurnal cycle with a maximum in the early morning when land based lightning is near its minimum. These features are also extant in the combined climatology constructed here.

Lay et al. [42] presented diurnal lightning statistics from World Wide Lightning Location Network (WWLLN) data, and these showed a larger range of regional peak times and amplitudes. A recent comparison between WWLLN and the National Lightning Detection Network (NLDN) over North America suggests that this difference stems partially from WWLLN's bias towards stronger flashes, partially from NLDN's limited sampling of lightning over the ocean, and remains partially other/unexplained [44]. In regions of overlap the NLDN diurnal cycle agrees closely with the OTD/LIS data. The global diurnal peak in lightning occurs in the late afternoon in all three data sets. The local time associated with DEMETER daytime overpasses is near the annually averaged diurnal minimum such that more lightning would be expected during nighttime DEMETER observations. This is contrary to tautology which puts more lightning during the day. Figure 8 shows some representative spatial plots of the combined climatology, for January and July 200 – 400 and 1400 – 1600 hours local time. The minimum flash rate shown has been artificially limited at 10^{-4} times the maximum flash rate to enhance details. The preponderance of lightning flashes over the land is immediately evident with the average land to ocean ratio being about a factor of ten. The effects of season is also evident with

the summer hemisphere showing lightning extending to higher latitudes. The features evident in Figure 8 are consistent with previous publications of the OTD/LIS data, e.g. [41].

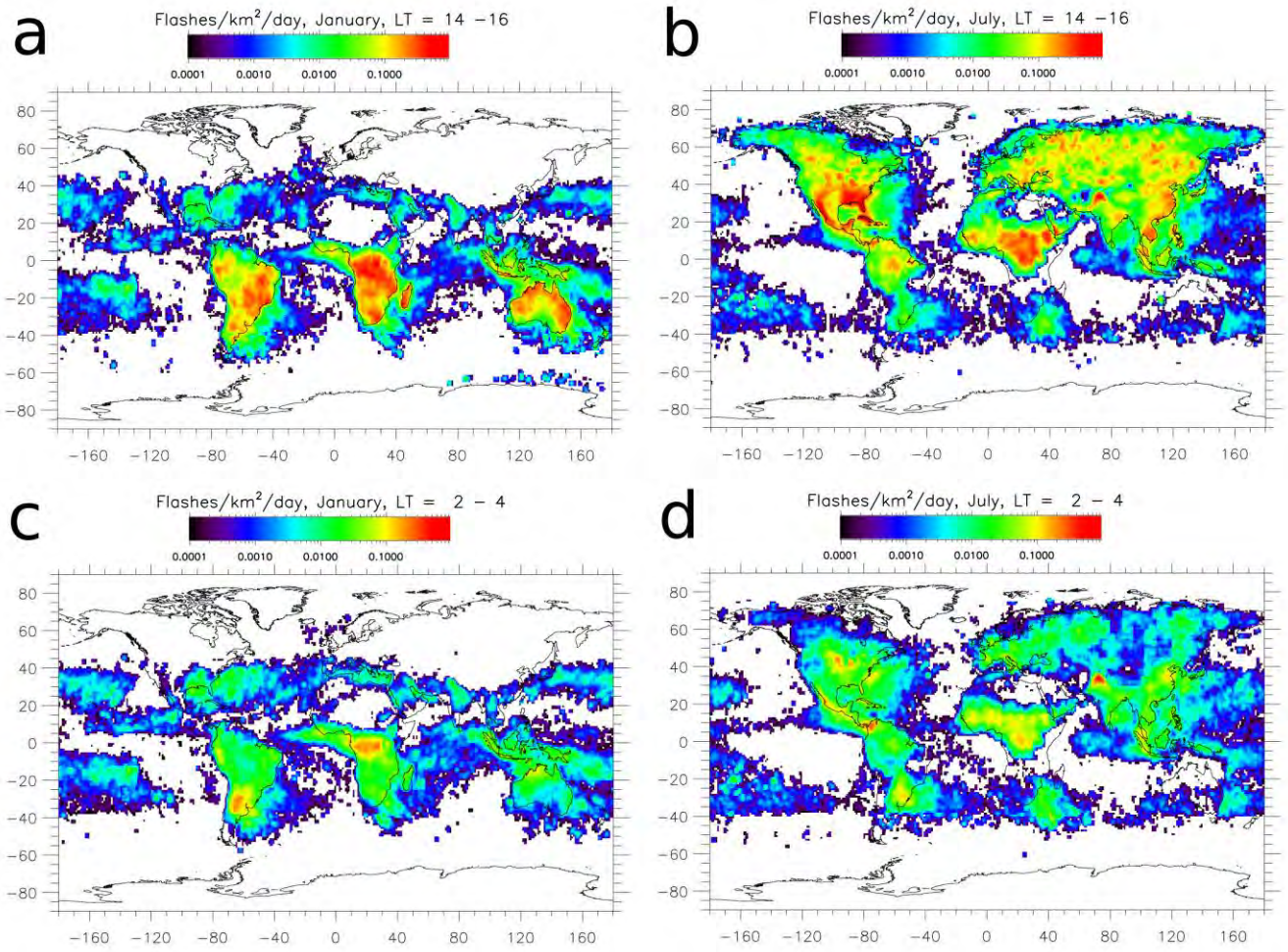

Figure 8. Representative Spatial Optical Flash Climatology

2.4 Interpreting the Wave Data

In order to constrain our initial model with measurements of VLF spectral density taken by the DEMETER satellite, the contribution of lightning to the DEMETER data set must be assessed and organized. The temporal and spatial dependencies of VLF from LGW in LEO are expected to be different from those of space based sources of VLF radiation such as plasmaspheric hiss. Lightning occurs predominantly over land, in the evening, and during summer. These are characteristics associated with terrestrial meteorology and are not expected to be shared by non-terrestrial VLF sources observed in LEO. In addition to considering the climatology of lightning in interpreting DEMETER measurements it must be considered that the VLF from lightning propagates up through the ionosphere before being detected. Conversion of VLF radiation in the earth ionosphere waveguide into whistler mode radiation beyond the ionosphere is a complicated process and depends in a non-trivial way on: the total electron and ion content and profile in the ionosphere, the dip angle and intensity of the geomagnetic field, the frequency of the incident radiation, and even the wave-normal of the radiation with respect to the ionospheric electron

gradient and geomagnetic field. Still, as a general rule there is more absorption at low magnetic latitudes, during the day, and at higher frequencies. These relationships are typically characterized by power laws [40]. It can be clearly seen in Figure 4a that the minimum VLF spectral densities at DEMETER altitudes occur right along the magnetic equator and not the solar equator as observed for lightning. We know that VLF trajectories in magnetized plasma follow field lines directly or indirectly. These observations confirm the importance of LGW conversion and attenuation in understanding the DEMETER observations and make the use of both magnetic and geographic coordinates essential.

Globally lightning peaks in July, so we expect VLF power from lightning to also show a peak in July. Looking for hemispheric trends, as indicated by Figure 7, is more complicated because ducted whistler radiation also shows up at the conjugate location, and even in the absence of a duct whistler propagation is strongly affected by the geomagnetic field and plasmapause location such that power may show up in the conjugate hemisphere at a similar apex latitude. As a first cut Figure 9a shows a plot of $\mu V^2/m^2/Hz$ vs. frequency for nighttime orbits and λ_A below 55°, Figure 9b shows daytime orbits and λ_A below 48°. Both figures show the data with monthly averages plotted in different colors where violet → red correspond to January → December. Higher Apex latitudes have been excluded because of strong non-lightning emissions there associated with auroral processes; also, as seen in Figure 8, the majority of lightning occurs at lower latitudes. The reason for the relatively lower latitude cutoff during the day is due to a combination of, diurnal variation of the auroral oval latitude and the relatively weaker spectral amplitude during the DEMETER daytime orbits making any contamination more problematic. In Figure 9a the blue trace representing March still shows features around 6 – 8 kHz possibly associated with high latitude processes.

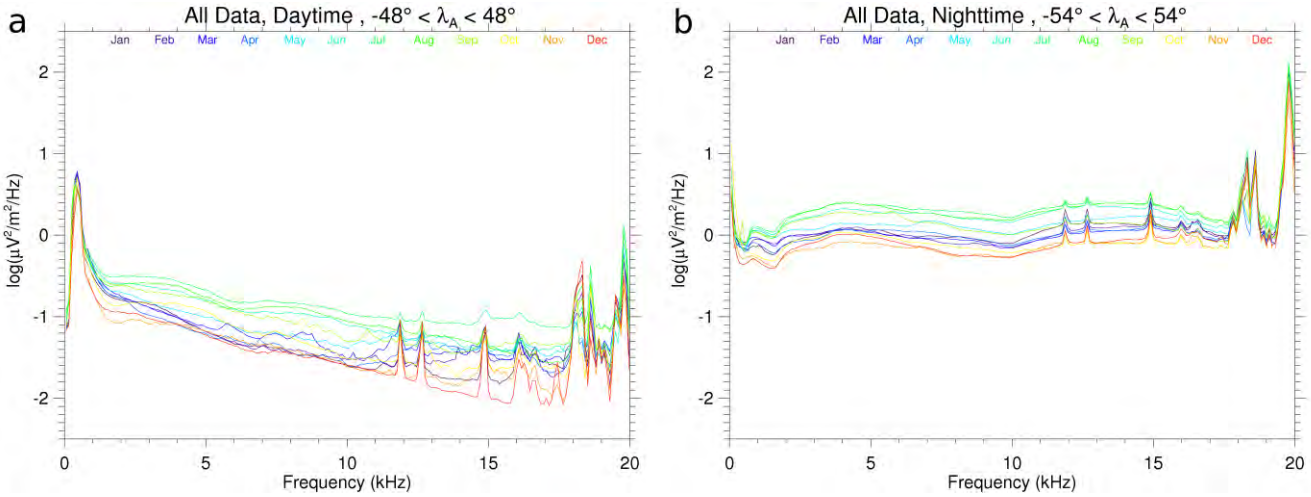

Figure 9. DEMETER Spectral Density vs. Frequency

There is a clear annual cycle evident in Figure 9 with maximum power being seen in July and August as expected for a lightning driven process. This annual variation is seen in both daytime and nighttime orbits with similar amplitude. The nighttime measurements show higher values by an order of magnitude or more, as expected given the larger occurrence of lightning, the higher altitude bottom of the ionosphere, and the smaller total electron content expected during DEMETER upward orbits. Both plots show a broad peak around 3 – 5 kHz consistent with

lightning after undergoing frequency dependent absorption in the ionosphere. The sharp peaks in the spectra are due to VLF transmitters and they show similar diurnal variation, but no additional annual cycle. The daytime orbits show a maximum below 1 kHz with little annual cycle which is consistent with a Hiss like emission. The nighttime feature in this frequency range does show the same annual cycle and so is likely driven by lightning. The flatness of the spectrum is surprising especially for the nighttime data and it is clear that the seasonality extends to high frequencies. If binned more finely these spectral features do show systematic latitudinal trends, but do not seem to depend strongly on proximity to an area of active lightning. Some additional discussion of these features is included below and in later sections but a full analysis is beyond the scope of the current investigation.

A cursory inspection of figures 4 and 8 show the general spatial correspondence of the DEMETER VLF data at 5 kHz with the OTD/LIS lightning maps below auroral latitudes, and Figure 9 confirms that the temporal variation is consistent with lightning as well. In Figure 10 a color plot of VLF spectral density is presented, again excluding high latitudes, as a function of longitude and frequency. The purpose here is to break down the range of frequencies which show a spectral and spatial relationship consistent with lightning. The months of January and July are presented separated into upward and downward orbits.

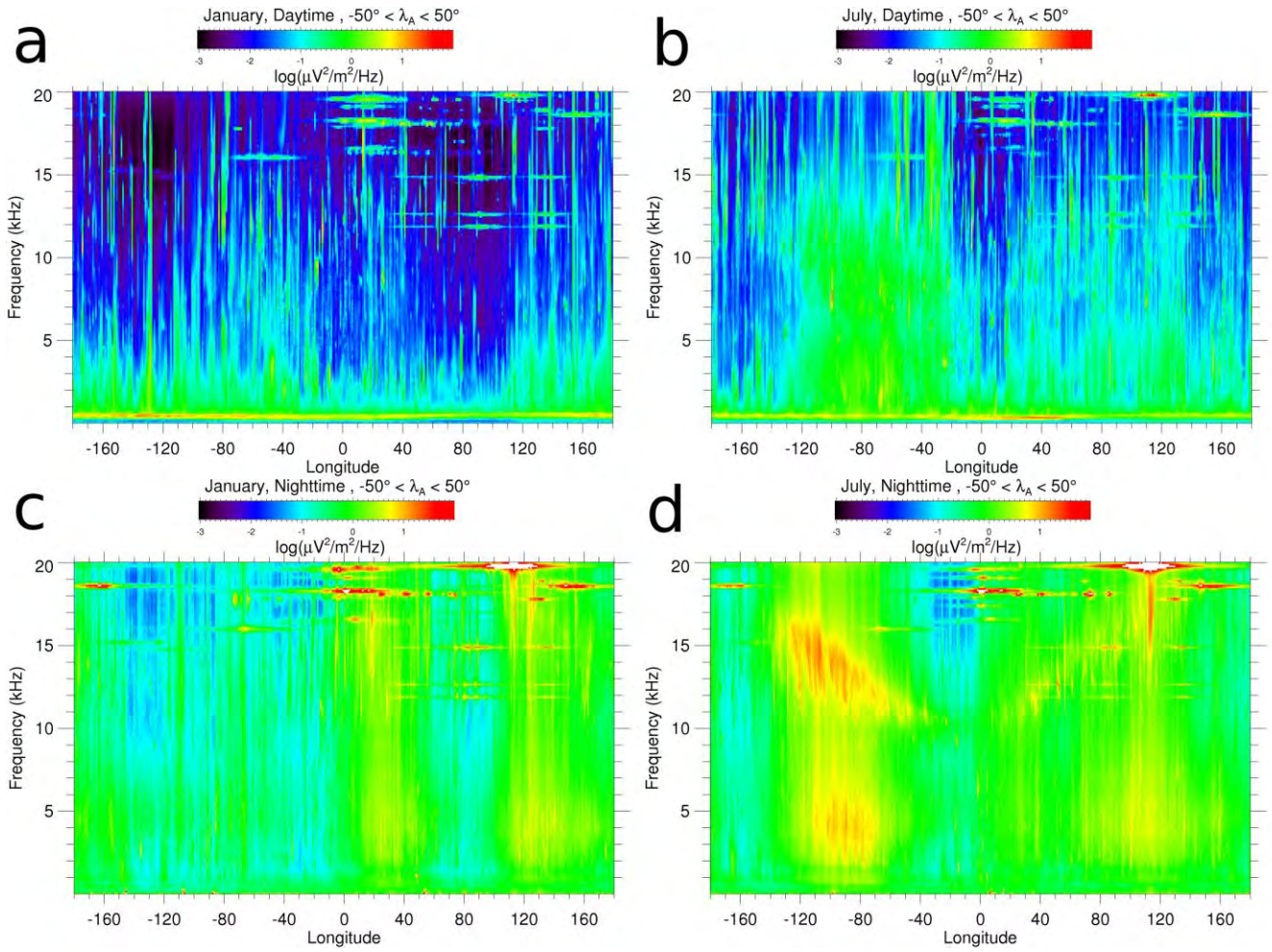

Figure 10. DEMETER Spectral Density, Frequency vs. Longitude

In Figure 10 a-d VLF transmitters show up as horizontal bands, with NWC being most prominent at a frequency of 19.8 kHz and 114° longitude (it also shows the spectral broadening observed previously, e.g. Parrot et al., [45]). The Hiss like emission below 1 kHz seen in Figure 9 shows up at all longitudes during the day. Overall the most evident features of Figure 10 show qualitative agreement with the spatial and temporal variation associated with lightning. More VLF spectral density is present during nighttime orbits, and in the northern hemisphere summer. There are major features associated with land masses in their summer hemispheres consistent with Figure 3. Figure 10a (January daytime orbits) shows the lowest magnitudes and very little in the way of systematic patterns, with the exception of the Hiss band already mentioned. Referring back to Figure 4a we see that a large fraction of the observations in Figure 10a are showing the effects of instrumental sensitivity and these have been averaged into the results shown. Figure 10 along with Figure 4 make it clear that the broad peak at 5 kHz seen in Figures 9a and 9b are strongly correlated to major landmasses and so lightning. This is also consistent with the seasonal variation shown there and the spectral content of lightning. The nighttime peak near 15 kHz shown in Figure 9b also correlates with the landmasses and shows an interesting frequency dependence as a function of longitude.

In order to investigate these features in more detail Figures 11 and 12 show similar plots (spectral densities for July and January respectively separated into upward and downward orbits as a function of frequency and longitude) now segregated according to magnetic hemisphere (apex latitudes between 15 and 50 for the Northern Hemisphere and -15 to -50 for the Southern Hemisphere). In these figures tropical latitudes have been mostly eliminated, and the scale has been adjusted in order to emphasize seasonal trends. Also included in Figures 11 and 12 are the averaged lower hybrid resonance frequencies (LHR) calculated from averaged plasma compositions estimated with the International Reference Ionosphere (IRI) combined with averaged geomagnetic field values from the International Geomagnetic Reference Field (IGRF). The most updated versions of these reference codes at the time of calculation were utilized (IRI-2007 and IGRF-2011). The local ion composition for 2007 was calculated with the IRI and the local geomagnetic field for 2007 was calculated with the IGRF (2007 was chosen because it was the latest year available for the IRI and it was the average year of the DEMETER data utilized), the middle day of the month was chosen for the local times relevant to the DEMETER overpasses. The calculation of the LHR frequency strictly follows that described in Brice and Smith [46], $\omega_{LHR} = \frac{1}{M_{eff}} \frac{\omega_p^2 \omega_H^2}{(\omega_p^2 + \omega_H^2)}$ where M_{eff} is the plasma effective mass, ω_p is the electron plasma frequency, and ω_H is the electron cyclotron frequency.

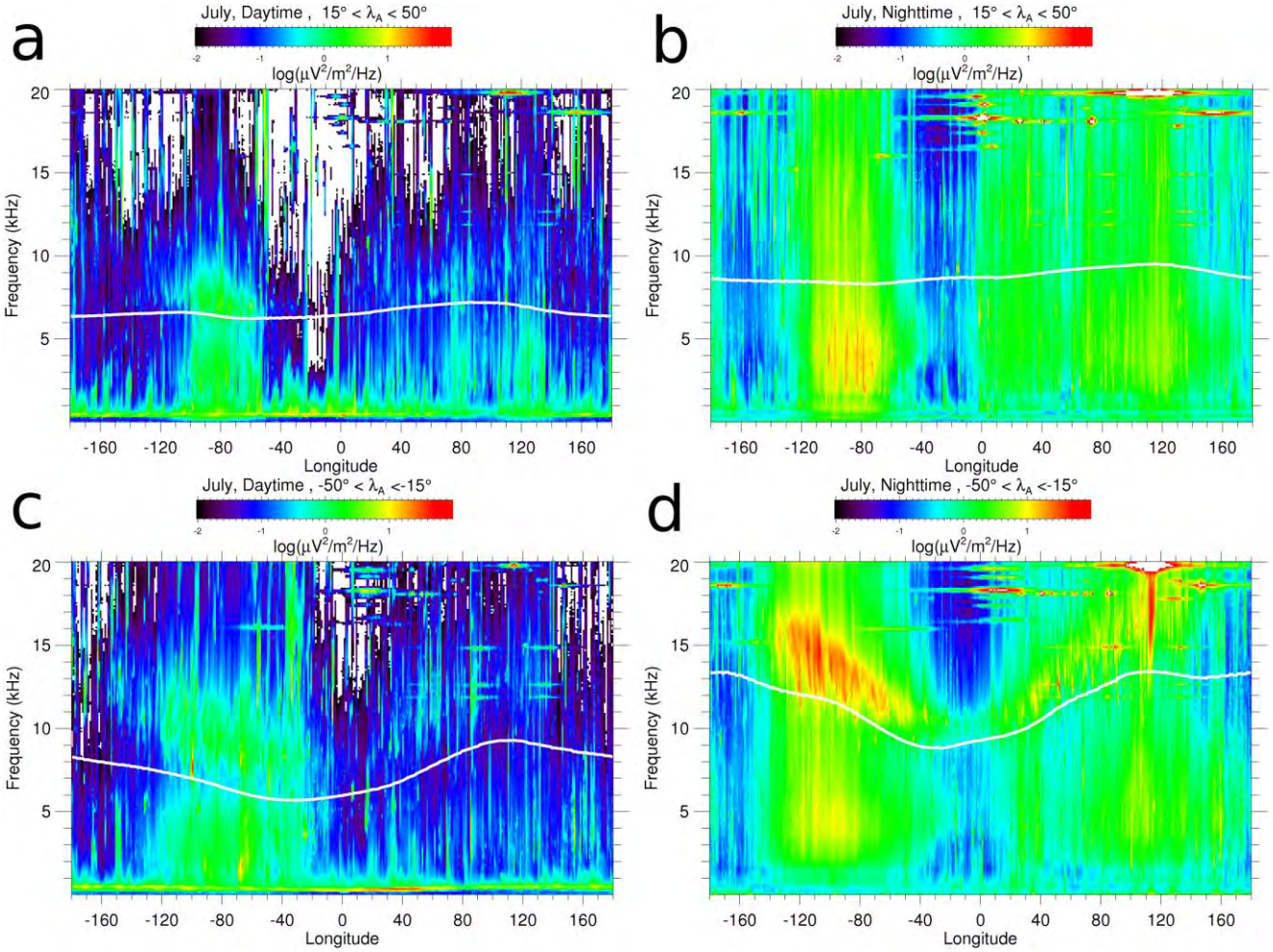

Figure 11. Hemispheric July Spectral Densities, Frequency vs. Longitude

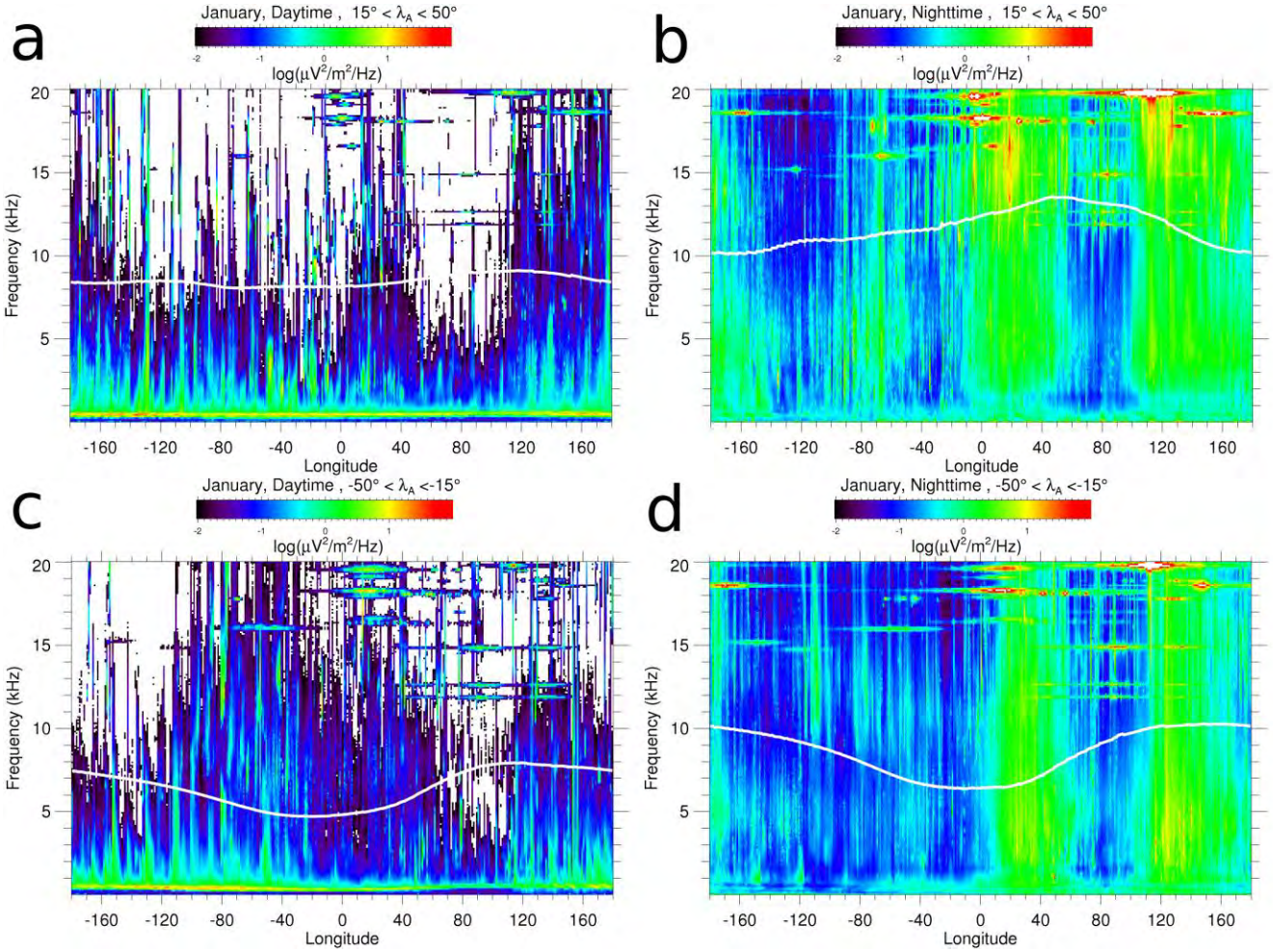

Figure 12. Hemispheric January Spectral Densities, Frequency vs. Longitude

Figures 11 and 12 again show major features consistent with lightning and present an explanation for the higher frequency waves showing an annual cycle in Figures 9a and 9b. They are consistent with the LHR Hiss described by Brice and Smith [46] and observed innumerable times since. In that work they are described as being generated in the immediate vicinity of the satellite, associated with nonducted whistler propagation from the opposite hemisphere, and exhibiting a lower cutoff at the LHR. This lower cutoff reflects the fact that the LHR its self defines a cutoff frequency for propagation transverse to the ambient magnetic field. Such quasi-resonant, quasi-electrostatic, whistlers can show a large increase in intensity close to the LHR as their group velocity decreases and they near magnetic reflection. Additional discussion of relevant LHR observations and theoretical treatments can be found in e.g. [21, 47, 48, 49]. Figures 11 and 12 show that the LHR emissions are associated with lightning in the conjugate hemisphere, so that Figure 11 shows maxima above the LHR in the southern hemisphere associated with lightning over North America and Euro/Asia in the northern hemispheric summer. The shift in the predicted lower cutoff of the LHR hiss band between day and night is consistent with the calculated values. Binning the results into smaller latitudinal regions results in good agreement between the shifting LHR and the lower cutoff frequency (not shown). In this first cut, single wave-normal component, climatological look at the data it is not possible to distinguish uniquely between the local quasi-resonant LHR hiss and a propagating quasi-

longitudinal wave above the LHR (e.g. a 0+ whistler, or a ducted 1- whistler). Knowledge of the total wave normal vector would potentially allow discrimination, or alternatively reliable observations of the magnetic field as the quasi-electrostatic waves have very little power in their AC magnetic fields.

Figures 9-12 show that the major features of the DEMETER VLF data set above 1-2 kHz can be explained either by lightning or auroral processes. This conclusion is consistent with previous work by Nemec et al. [50]. The spatial, annual, and diurnal features have all been explored and along with spectral properties are found to be consistent with lightning. Although only one wave normal component is represented in the data theoretical predictions and satellite observations confirm that the wave vector is near vertical within the ionosphere e.g. [51], at least for 0+ whistlers, and so we expect the measured component to capture most of the field intensity. In any case in concert with the IGRF or the satellite ephemeris we know the angle between the wave vector and the local geomagnetic field and so could reconstruct the full intensities from the polarization ratios. Nemec et al. [50] also concluded that DEMETER survey mode data "represents a sufficient proxy for the intensity of electromagnetic waves". This data set then, provides an excellent benchmark for a climatology of lightning generated VLF in LEO constructed by other means.

2.5 VLF from Lightning in the Earth-Ionosphere Waveguide

The lightning climatology employed here has already been outlined in section 4, it originates from impulsive optical measurements taken from space and can be specified in flashes/km^2/day as shown in Figure 7. Our objective is to construct a climatology of VLF radiation from lightning in low earth orbit, so we would like to convert flashes/km^2/day in the troposphere to Power/km^2/Hz at LEO. The initial approach taken here assumes that the number of flashes/km^2 is proportional to the amount of power/km^2 radiated in the VLF. This is equivalent to saying that the strikes are incoherent and the distribution of power over all strikes is the same as a function of time and place. There is some evidence to suggest that this is not quite the case as, for example, the diurnal cycle of flash number is quite different over oceans [43] and so might be the power distribution [52]. Initial studies of seasonal variation in the charge moment distribution functions for intense lightning indicate overall similarity to the total [35]. However, there are also suggestions that the temporal/spatial variation of powerful strokes is somewhat different than that of the entire range of powers as touched on in Section 4 and alluded to in Lay et al. [42]. While it would certainly be of interest to include a spatially and temporally dependent flash to power conversion factor there is insufficient guidance on this point in the literature to do so at this time.

Once the spatial and temporal distribution of VLF power generation from lightning has been fixed it is still necessary to propagate that power within the earth-ionosphere waveguide and then couple it into whistler mode radiation at the bottom of the ionosphere. At the most general level we expect power spreading in free space to drop off as the square of the distance due to purely geometric considerations. Because the conductive ground and conductive ionosphere form a spherical waveguide for VLF radiation, at the next level of abstraction we expect that attenuation will transition to an inverse distance proportionality as distance increases, and show a pronounced frequency dependence. At even longer distances we expect to see some focusing occur because the earth is round and rays diverging from an initial point will start to converge at

the antipodal point. The exact details of how power in the waveguide couples to the whistler mode are still obscure, and preliminary studies suggest that modeled electric fields are more than 10 times smaller than in situ measurements in the lower ionosphere [53].

Rocket and satellite observations show that sferics can couple to the whistler mode over distances of at least 1000 km from the flash [32, 33, 51]. In the most complete study of its kind Fiser et al. [54] analyzed ~30000 lightning whistler pairs and found that the average amplitude of a whistler is largest when the magnetic footprint of the detecting satellite is approximately 1 degree north of the causative lightning location. The spatial resolution of this study was 1 degree in latitude and all comparisons were made in Europe. This distance is significantly different than the vertical projection of the satellite location, which would be about 4 degrees north of the magnetic projection at the location in question. For distances in the range of 300-2000 km they found that the mean whistler amplitude in LEO drops off in inverse proportion to the distance from the location of maximum amplitude. In light of these studies we utilize an inverse square relationship between a flash location and the power it delivers to the ionosphere. A more complete treatment might transition from the inverse square treatment utilized here to the dB/Mm treatment more familiar to radio engineers at some distance from the flash.

In the future it would be of interest to study the frequency dependence of whistler energy as a function of distance from the flash location. Ferencz et al. [55] report the observation of "Spiky Whistlers" in LEO which they attribute to the formation of a whistler from a tweek, a tweek being a sferic which has traveled far enough in the earth ionosphere waveguide to become dispersed at a frequency consistent with the cutoff frequency of the waveguide, 1.5 – 2 kHz, and its harmonics. This demonstrates that the frequency characteristics of the generating sferic can be transferred onto the whistler. It is well known that the frequency characteristics of sferics change greatly as a function of distance from the flash. Such changes are often described in the context of a mode theory for waveguide transmission, as described in [56]. To summarize: frequencies around and below 5 kHz are attenuated significantly relative to higher frequencies which then appear enhanced in the resulting spectrum. During the night this relative maximum in attenuation shifts somewhat lower in frequency due to the taller waveguide, and overall attenuation is lower due to the smaller ion/neutral collision frequency at that higher altitude. Sferics which cross the day/night terminator will experience an additional loss due to the abrupt change in waveguide height. Measurements taken nearer to a flash, and/or specifically designed to measure it's incipient spectrum, show a peak around 3 – 5 kHz and a drop off well described by one over the frequency out into the MHz range [57]. These two competing characteristic (incipient spectrum and transport) lead to a typical measured spectrum in the earth-ionosphere waveguide which peaks around 10-15 kHz (Dowden, Brundell, and Rodger [58] suggest that half power frequencies of 5 and 19 kHz are reasonable). Spectra of this type are readily available on the web, including many associated with the WWLLN network (webflash.ess.washington.edu). This description is also borne out by a recent publication on the development of a typical waveform bank for use in the VLF geolocation of lightning [34] which incorporates thousands of measured spectra at various distances. The Fourier transform of Figure 3 in that paper (which shows expected received waveforms as a function of distance from the stroke) would give typical spectrum as a function of distance from the flash consistent with the above expectations (Said, private correspondence).

In this work the conversion from flashes/km^2/day to power/km^2/day proceeds as follows. For a given location it is first assumed that the number of flashes/km^2/day converts directly into a power/km^2/day at that location (P_0 in equation 1). Then contributions from every other location are calculated based on a reference distance reflecting the length scale of the contributing grid location (geocentric coordinates are not equal area) and a great circle distance between the grid centers, an additional normalization is included to account for the difference in areas between the two locations and so conserve the per km^2 designation.

$$P_1 = P_0 + \sum_{i=1}^{n} P_i * \frac{referencedistance^2}{greatcdistance} * \frac{area(i)}{area(0)} \qquad (1)$$

A limit on the great circle distance which can contribute to a location has not been included at this time nor has antipodal focusing. This calculation is done in universal time and then converted to local time. Figure 13 shows representative plots of the output which we refer to as pseudopower for January and July 1100 and 2300 hours local time. The units are arbitrary but the calculations were done conserving relative values per day and per km^2. In Figure 13 we have multiplied by the grid area at each location (giving units of pseudopower/day) in order to emphasize features related to the spatial distribution of power rather than the unequal area of our geographic grid which gets quite small at high latitudes.

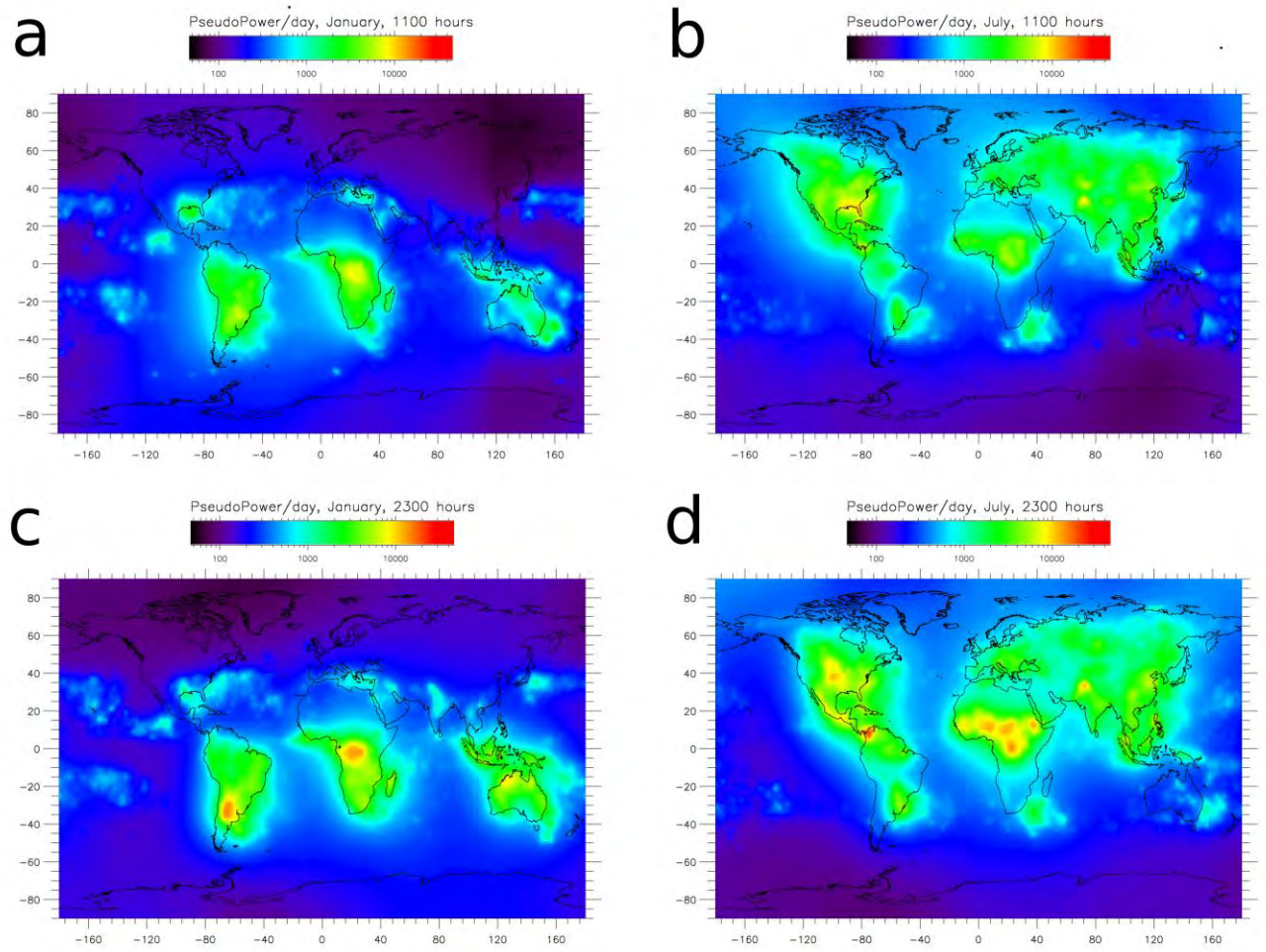

Figure 13. Representative Spatial Pseudopower Climatology

Attenuation of VLF energy in the earth ionosphere waveguide is often discussed in terms of dB/1000 km, e.g. [56, 59] with typical values being a few dB/Mm. Our inverse square treatment with reference distances around 100 km (1° geographic) drops off very rapidly at first, a factor of 100 in the first 1000 km corresponding to 20 dB/Mm, then more slowly equivalent to 2.5 dB/Mm in the 4th 1000 km. Over the first 10 Mm the intensity drops off by 10^{-4} corresponding to an average attenuation of 4 dB/Mm. At longer distances the attenuation becomes even smaller ~1 db/Mm in the 10th 1000 km. So, while simplistic, the inverse square treatment provides a good first cut and for our purposes is superior to a pure dB/Mm approach.

As noted above the initial spectrum of lightning is thought to peak around 3 – 5 kHz and then drop off as one over the frequency out to at least the 20 kHz considered here. Considering that the peak spectrum moves to higher frequencies with distance, and that empirically the power of a satellite detected 0+ whistler drops off as 1/distance^2, it is reasonable to adopt a generic spectrum shape extracted from Lauben, Inan, and Bell [24] and given in Equation 2, which shows a broad peak between 2 and 6 kHz. In Equation 2, ω is the angular frequency while a and b are constants (here a = 5000 and b = 1000). It is normalized over the frequency range of interest (0 - 20 kHz) before application to the pseudopower distributions.

$$f(\omega) = \frac{\omega^2(a-b)^2}{(\omega^2+a^2)(\omega^2+b^2)} \quad (2)$$

2.6 Transionospheric Attenuation

Once we have a VLF power spectrum in the earth ionosphere waveguide we must approximate in some way the leakage into the ionosphere and the attenuation as the wave energy propagates in the plasma. Here we will use the Helliwell curves (figure 3-35 in [40]), which are calculated employing refractive indices from the quasi-longitudinal approximation to Appleton's equation. Helliwell's calculations assumed a specific form for the average electron density and collision frequency profiles in the ionosphere, for daytime and nighttime conditions separately. Then the path integrated absorption was calculated through the ionosphere for vertically incident radiation of 2 and 20 kHz at a range of geomagnetic latitudes above 10°. In our application absorption for intermediate frequencies are estimated assuming that absorption is proportional to the square root of the frequency.

The validity of the Helliwell approach is checked in some detail by Tao, Bortnik, and Friedrich [60], who find reasonable agreement with a more numerically intensive full wave calculation coupled to more modern values for the electron density and collision frequency profiles. Lehtinen and Inan [61] also present state of the art calculations which are compared to other Helliwell based calculations performed by other researchers. The main limitations associated with application of the Helliwell curves are twofold: first, the quasi-longitudinal approximation upon which they are based is known to fail for large values of the geomagnetic inclination angle such as exist near the equator; and second, the ionospheric profiles employed, while reasonably representative, do not show the range of systematic variation now known to exist in time and space (as summarized by e.g. IRI). Nevertheless the Helliwell curves provide a widely accepted baseline from which to proceed. The difficulty of using updated absorption values is due in part to the wide variety of variables that transionospheric absorption will depend on, including geomagnetic inclination angle, geomagnetic field strength, electron density and collision profile. Each of which have their own spatial and temporal dependencies. Thus in our application we would like to have an average absorption calculated for climatological averages of each two hours in local time, each month, each frequency, at each spatial location.

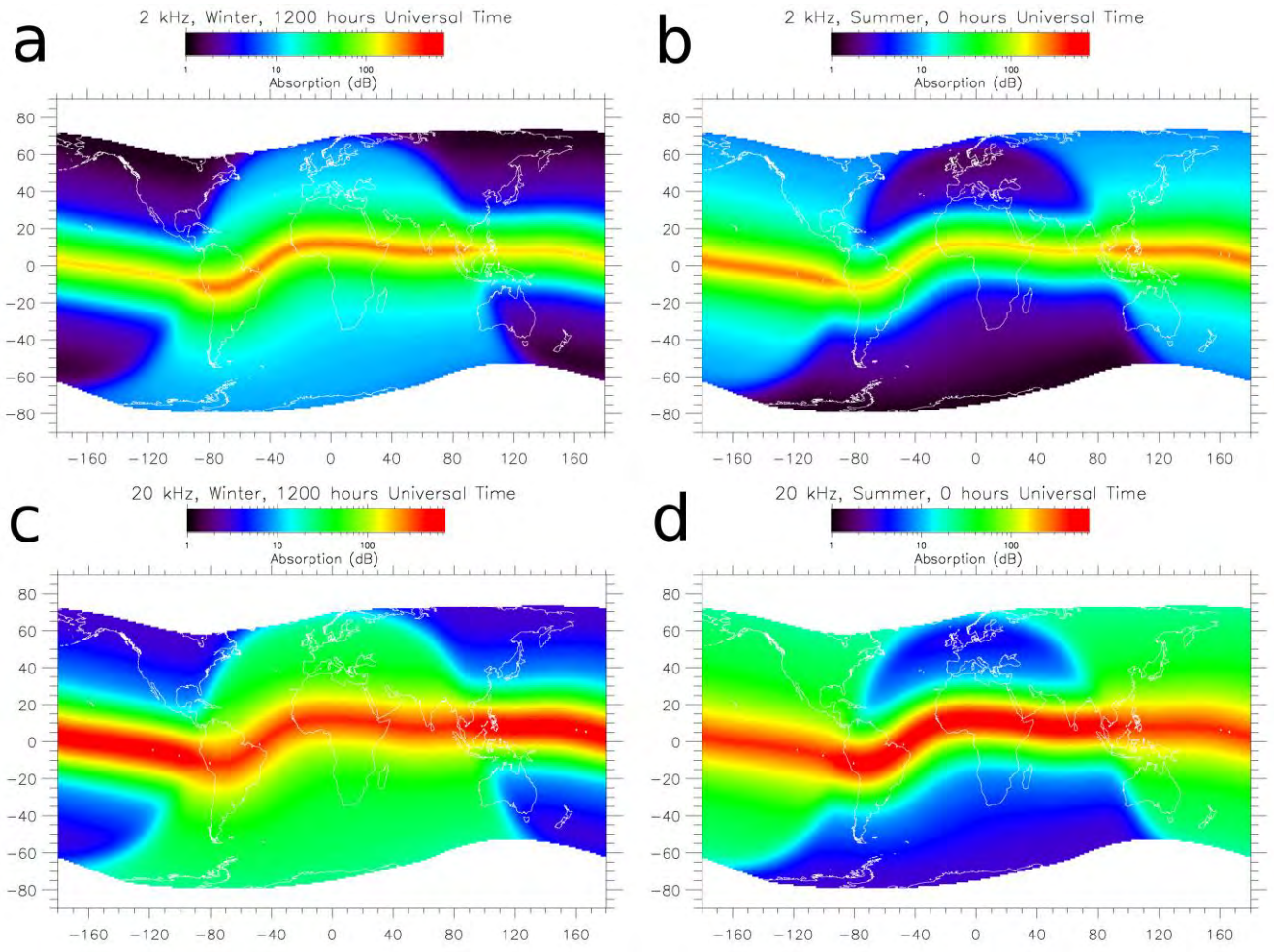

Figure 14. Transionospheric Absorption, Representative Spatial Climatology

In our particular application the absolute values of the absorption are not as important as the relative values, and so details such as polarization loss (3 dB), reflection (1-2 dB), and whistler coupling factor (discussed in e.g. [24]) while potentially important are not examined in any detail. Our values are taken directly from Helliwell [40] Figure 3-35. Figure 14 shows some representative global transionospheric absorption plots at 2 and 20 kHz for winter and summer at noon and midnight. Temporal transitions are handled heuristically in a manner similar to Starks et al. [18], involving an inverse tangent function of the solar zenith angle at D region altitudes. In local time coordinates there is no longitudinal dependence to the Helliwell curves and so, for example, the appropriate curve to apply to Figure 13a at 2 kHz would be a longitudinal section of Figure 14a at -15° longitude, and 13c at 20 kHz would take a longitudinal section of figure 14c at 165° longitude.

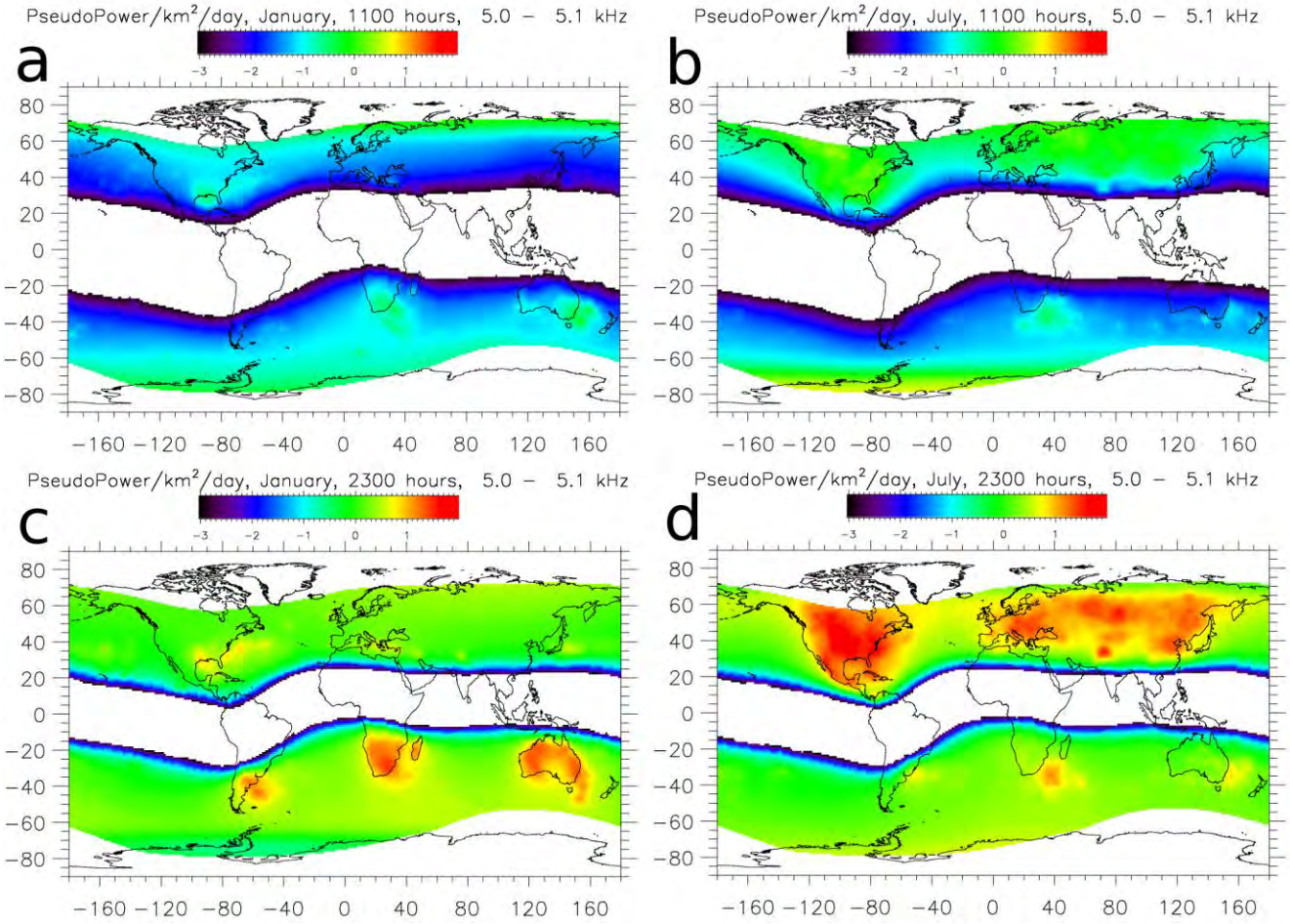

Figure 15. Pseudopower in Low Earth Orbit, Representative Spatial Climatology

Figure 15 shows the results of applying the appropriate Helliwell absorptions at 5 kHz to the pseudopower distributions shown in Figure 13. The values have been normalized to a maximum of 100 and plotted as log(pseudopower/km^2/day) to facilitate comparison with Figure 3. Similarity to the DEMETER data shown in Figure 3 is readily apparent as are some differences. The most glaring differences include the wide empty area near the equator (both Figure 3 and 15 show a dynamic range of 5 orders of magnitude), the lack of power in the conjugate locations, and the lack of any auroral power spectral density. Part of the equatorial difference can be ascribed to the failure of the longitudinal approximation there and so the validity of the Helliwell curves. Another part is related to the second point; propagation of VLF radiation is coupled to magnetic field lines. We expect to see power spectral density near the conjugate locations of strikes, but we also expect power spectral density to be displaced along field lines (i.e. equatorward) on its travel from the ground to the satellite location. This effect has been observed previously in DEMETER data, e.g. [54], and will tend to fill in the blank areas near the equator. Though transionospheric absorption was applied, Figure 15 still represents locations within the earth ionosphere waveguide.

2.7 Magnetospheric Propagation

As previously discussed both ducted and non-ducted propagation of whistler waves in the magnetosphere have been observed, or inferred, and both are thought to be important in different contexts. Ducted propagation follows field lines and so, to first order, power at a given apex latitude shows up at an equivalent conjugate latitude with frequency dependent temporal dispersion and little damping. Non-Ducted propagation is more complex showing a strong coupling between spatial and spectral dependencies. Power input at a given apex latitude can show up at either a relatively higher or lower conjugate latitude depending on frequency. In the current treatment only ducted propagation will be explicitly handled, though it would certainly be of interest to extend this work to non-Ducted propagation. We handle it as follows: field line trajectories were calculated at each corner of a 1°x1° geocentric grid as discussed for the apex latitude calculations; pseudopower was calculated within each grid location; the pseudopower was assumed to remain within the flux tube defined by the corners of each grid and transported to different altitudes within the apex coordinate system; in order to retain per meter squared units the pseudopower was scaled by the changing cross sectional area of the flux tube at any altitude. Because we are interested in comparing to DEMETER data, an altitude of 660 km will be focused upon here along with its conjugate location, but values are available anywhere along the field lines.

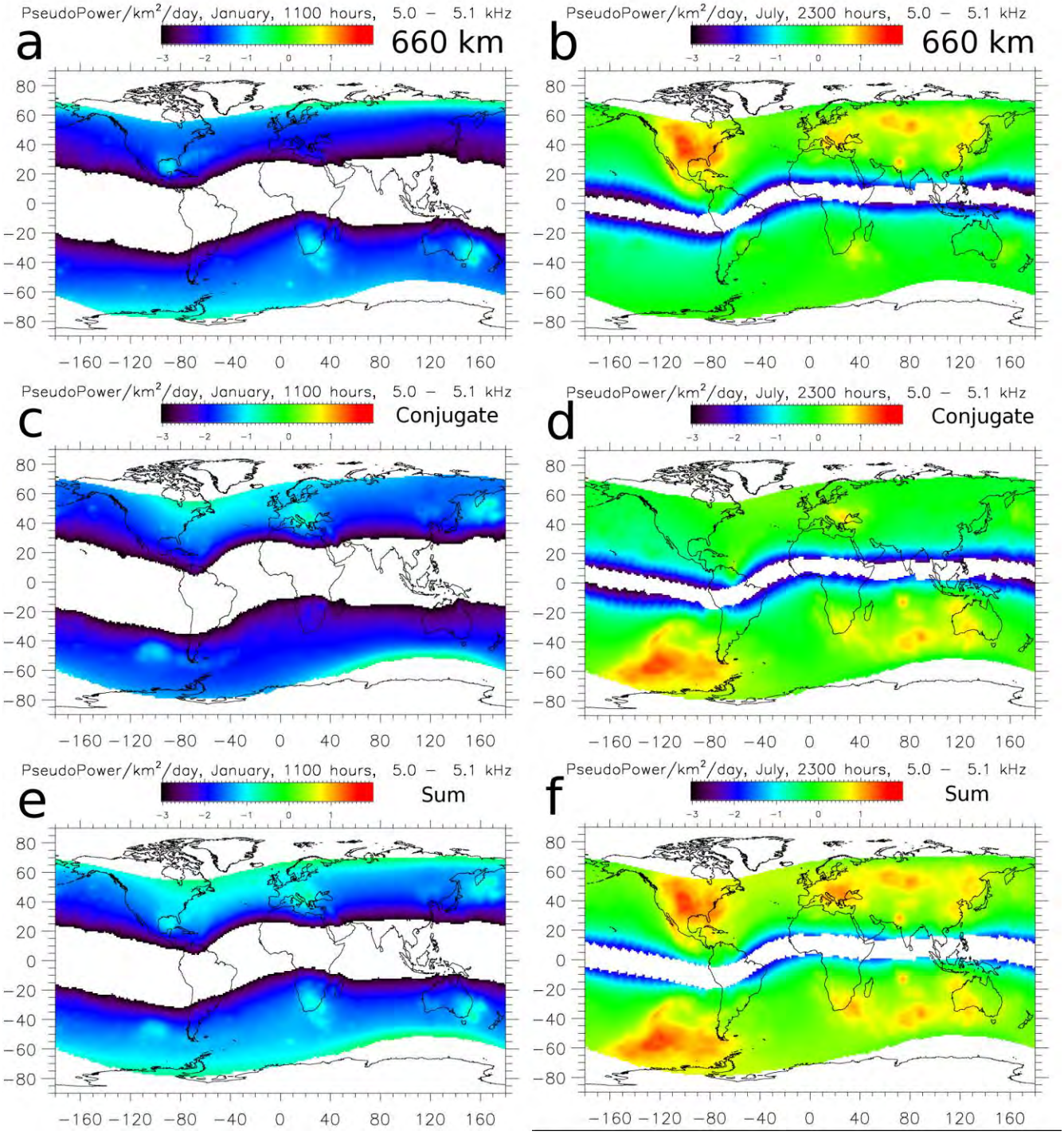

Figure 16. Pseudopower Climatology in Low Earth Orbit, Magnetospheric Propagation

Figure 16 shows results of the ducted transport calculation applied to the pseudopower distribution after Helliwell attenuation shown in Figure 15 for January 1100 hours local time and July 2300 hours local time. Note that we have mapped the values from apex coordinates back to a 1°x1° geocentric grid at the altitude in question. Along with the model at 660 km (Figure 15a and 15b) and the conjugate location at 660 km (Figure 15c and 15d) we also show an average of

the two. At a first cut we think that the ducted model is appropriate here in part because DEMETER sees a lot of power at 5 kHz in the conjugate region of the North American continent (Fig. 4d). In general for non-Ducted propagation we would expect frequencies below the LHR maximum along the trajectory to undergo magnetic reflection before reaching 660 km. As shown in Figure 11 and 12 there is significant power with the spatial temporal signature of lightning below the LHR frequency in the assumed conjugate region. There is almost no lightning below that area which could generate 0+ whistlers at the observed average spectral densities. It is also possible that the observed radiation is still propagating in the longitudinal mode and, although nonducted, has not yet become oblique enough to undergo magnetic reflection. This topic is beyond the scope of the current investigation and is subject to continued study.

Figure 15e and 15f show a marked resemblance to Figure 3a and 3d respectively. Outstanding are the existence of very low values near the equator in the night time summer, which does not show up in the DEMETER average data, and that the data with intensity below -3 $\log(\mu V^2/m^2/Hz)$ in January daytime is somewhat broader in longitude especially near 30° and 135° longitude. While we have used -3 $\log(\mu V^2/m^2/Hz)$ as the lower limit in our DEMETER plot Figure 4 and subsequent discussion shows that many of the averaged January values seem to be affected by the instrumental noise floor and/or sensitivity. It is likely more appropriate to consider any value below -2.5 $\log(\mu V^2/m^2/Hz)$ or even higher to be noise in this context.

In general lightning locations are driven by storm locations, and while their occurrence can be described climatologically, specific storm and flash locations are stochastic events. So even if VLF intensities as measured by DEMETER were entirely due to lightning, and OTD/LIS were 100% accurate and precise, and our model sufficiently captured all features of the conversion, we do not expect a one to one correlation between DEMETER data and our model. It is worth noting that the 20-30 observations, representing 800-1200 individual spectrum, per grid location per month still only represents around 30 minutes of integrated dwell time. Also the OTD data we are comparing to have undergone additional smoothing in order to show more continuous features. For example the HRMC represents a 2.5° moving average applied to each 0.5° grid, while the LRADC involves a 110 day moving average centered on each day of the year. We have not applied this level of smoothing to the DEMETER data. Nevertheless, it seems that many of the gross features of the DEMETER survey data can be explained on the basis of this relatively crude analysis.

2.8 Scaling the Model to DEMETER Observations

The previous analysis has shown general agreement between the pseudopower model and the averaged DEMETER survey data when considered in the appropriate light. We will now consider how best to scale the pseudopower climatology to the DEMETER observations. We know that not all of the spectral density in the DEMETER data represents LGWs, and we know that many salient features of the transformation from sferic to LGW at LEO are being treated here in a less than ideal fashion. Nevertheless, we will assume here that if the pseudopower climatology is representative of the contribution of LGW to VLF intensity at LEO then they should scale linearly. That is, the pseudopower climatology is currently on an arbitrary scale, we would like to convert it to real units with a single scaling factor which would be applied everywhere; e.g. pseudopower units * 100 = $\mu V^2/m^2/Hz$. Because we have been presenting the

data on a log scale this is equivalent to an additive scaling in log units; e.g. log(pseudopower units) + 2. = log($\mu V^2/m^2/Hz$).

In determining this scaling factor we would like to only include observations where LGWs dominate. Low frequencies where Hiss dominates should be excluded, as should frequencies above the LHR where quasi-electrostatic waves may dominate; from figures 9 – 12 and similar 2 – 9 kHz seems reasonable for nighttime and 3 - 7 kHz for daytime. High latitude observations where auroral phenomena occur should also be excluded. As in Figures 10 – 12 we choose an apex latitude of 50° as a spatial cutoff for auroral phenomena. However in the DEMETER data apparently auroral processes penetrate to lower latitudes at lower frequencies and during the day. These strong fluxes bias the scaling factor such that we have used a lower cutoff of 4 kHz for nighttime and 5 kHz for daytime. This choice represents a compromise between excluding all auroral phenomena and including regions where we expect lightning to be important. In addition we would like to be cognizant of known weaknesses in our modeling approach. The longitudinal approximation invoked in the Helliwell calculations breaks down for small dip angles and so we exclude apex latitudes below 20° from our determination. Observational limitations such as the sampling density relative to the signal variability and the effects of an instrumental cutoff should also be kept in mind. Finally, the correlation will be computed with DEMETER data averaged over a 2.5° spatial resolution, in order to smooth over some of the stochastic spatial variation in strikes and to promote overall similarity to the smoothing applied to the optical flash data set.

Within the set of data limited as described above we calculate a scaling factor from the fraction of data representing relative rank 0.6 – 0.9 by spectral density. This last will help to exclude outliers and minimize the contribution of the instrumental cutoff, while emphasizing locations where there are many 0+ whistlers (as seen in Figure 4). Because we are considering the correlation between log scaled data the importance of the higher ranks are magnified. Figure 17a shows the scaling factors for each month of the year at selected frequencies, day and night. Figure 17b shows the associated correlation coefficients between the data and model.

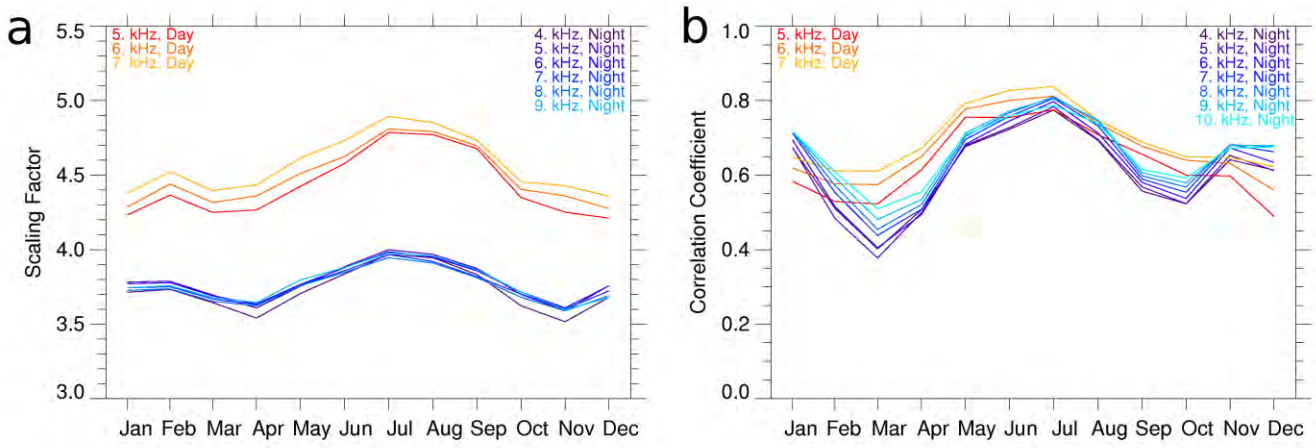

Figure 17. Climatology Scaling Factors and Correlation Coefficients

Figure 17a reveals a systematic temporal variation in the scaling factor, with a large peak in Northern summer and a smaller peak in Southern summer. This is due at least in part to the

overly simplified transionospheric attenuation treatment where only the solar zenith angle as a function of time defines a season. It is well established that the ionosphere has a distinct seasonal cycle which we are ignoring here. The same monthly trend is evident day or night. It is also clear that the daytime and nighttime values fall within different distributions, and the scaling factor is roughly an order of magnitude higher during the day. That is, given only a single scaling factor based on nighttime data, the model would underestimate the spectral densities by a systematic factor during the day. This most likely relates to our simple transionospheric transfer function, but could also have a contribution from the OTD/LIS data that our model originated from, which might show different sensitivities between day and night. The correlation coefficients shown in Figure 17b reveal a very similar temporal variation. This suggests another possible contributing factor to the monthly trend: there is increased lightning activity at high latitudes during summer, while more lightning is equatorial near the equinox (driven by the solar zenith angle differences between the seasons). Lightning at high latitudes is converted to LGW more efficiently (due to higher magnetic dip angle, smaller electron column densities, and possibly additional ducts), which provides a larger signal above background and mitigates some of the stochastic component in the signal. Overall, the correlation coefficients shown in Figure 17b reveal values consistent with a significant relationship between the model and the data, while still not accounting for all of the variance.

It would have been preferable to have a single scaling factor between the pseudopower representing our model and the DEMETER spectral density, but Figure 17a shows that it is inadvisable. This is not unexpected given the first cut treatment given here, but may still be achievable in the future. At minimum different factors should be used for daytime and nighttime, but given the apparent systematic nature of the monthly trends in both the scaling factor and correlation coefficient across frequencies and local time it seems reasonable to use a different scaling factor for each month, day and night. The final values are averaged over relevant frequencies and shown in Table 1.

Table 1. Frequency Averaged Scaling Factors

	Jan.	Feb.	Mar.	Apr.	May	June	July	Aug.	Sep.	Oct.	Nov.	Dec.	Mean
Day	4.30	4.44	4.32	4.35	4.52	4.65	4.83	4.81	4.70	4.40	4.35	4.28	4.50
Night	3.75	3.76	3.67	3.61	3.76	3.86	3.97	3.94	3.84	3.69	3.58	3.71	3.76

4. DISCUSSION

Figure 18 gives an overview of the model values compared to the DEMETER averages for 5 kHz, day and night, January, April, July, and October. The equatorial region is clearly in need of a better treatment of transionospheric attenuation and/or sferic to LGW transformation, especially at night. This fact is consistent with the breakdown of the longitudinal approximation there, but also likely represents the need for a seasonally varying ionosphere and perhaps adjustment for the known heterogeneity of the equatorial ionosphere (e.g. scintillation and plasma depletions). In the recent reanalysis of the Helliwell curves [60] the only glaring difference between the original curves and the recalculated values based on the IRI and a full wave model is a flattening out of the absorption for nighttime values below 20° latitude (Figure 5 in that work), and such an adjustment would certainly improve the agreement but still not close

the gap entirely. The need for an improved earth-ionosphere waveguide can perhaps be seen in the regions away from active lightning. As one moves longitudinally away from an active lightning region along a specific apex latitude the DEMETER data seems to drop off more quickly than the model. This could be driven by absorption in the waveguide, or alternatively by the increasing obliquity of the wave with respect to the ionospheric plasma gradient with increasing distance from the stroke. In addition our simplified treatment implicitly assumes that the spectrum of the sferic does not change with distance, which is not true at least within the waveguide as discussed previously. An initial look for regions where this effect might be important (e.g. over the Pacific Ocean) surprisingly revealed no large differences in spectrum.

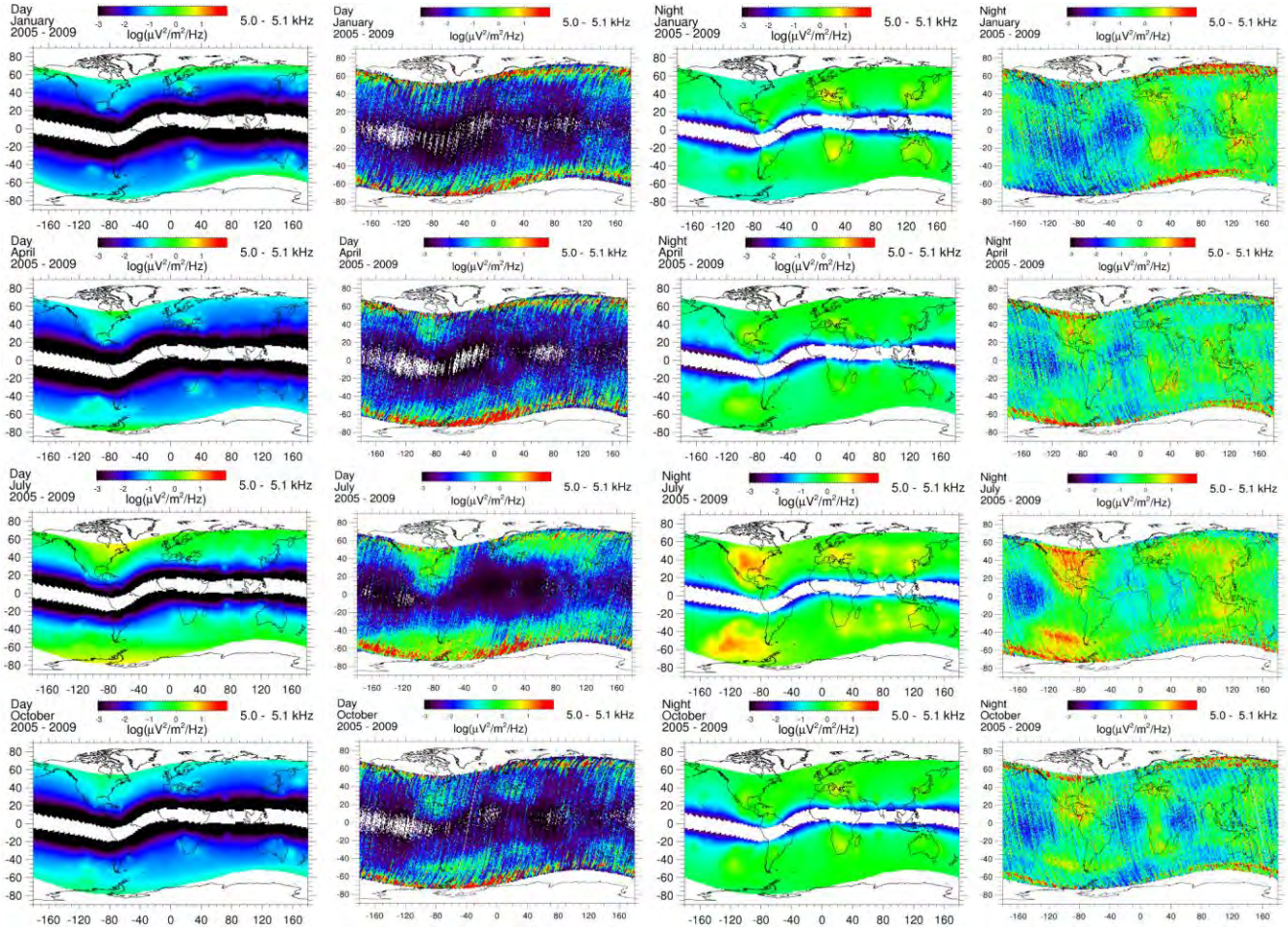

Figure 18. Spatial Plots of the Scaled Climatology and DEMETER Averages

The stochastic nature of lightning and storms relative to satellite observations is also evident in Figure 18. Even within regions of high lightning activity the model is smooth. The values originate in a highly smoothed OTD data set and become even smoother due to our inverse distance treatment. While a more detailed waveguide treatment may improve the model it will still introduce a similar smoothing effect. In order to capture the heterogeneity of the DEMETER data it would be necessary to treat individual storms as events lasting a finite time and lightning as a stochastic process where an individual stroke was drawn from a representative power distribution. In addition the conversion from waveguide power to LGW power may have a stochastic, or at least a spatial and temporal, component as it may depend on local variations in

the ionosphere (e.g. horizontal gradients in electron density), geomagnetic dip angle, or distance traveled in the waveguide. Even if these approaches were implemented it would still be necessary to model the satellite as sampling this distribution as it orbits. That is, even with a mission like DEMETER where survey mode data was captured almost continuously for five years, each 1°x1° location was only sampled for roughly 30 minutes in any given month. There was a large range in the values over a specific location for a given overpass, and this can be seen in the almost vertical striations observed in the DEMETER plots. These variations must depend in part on whether there was active storm below the satellite or at some distance, and when individual strikes were integrated into the survey mode average spectra. We are implicitly assuming that the true distribution was sampled sufficiently but it would be of interest to test that assumption.

Our climatology also extends to local times not sampled by the DEMETER mission. Figure 19 shows the spectral density at 5 kHz plotted vs. apex radius for some of our local time bins with color representing different months of the year where violet → red corresponds to January → December. It is interesting that Figure 19f, which overlaps with the nighttime DEMETER orbit, also has the most spectral density. This reflects a combination of flash density and ionospheric attenuation. Typically the peak spectral density was in the 2000 – 2200 hours local time bin for a given apex radius, frequency, and month. This is expected as it contains the peak flash rate (Figure 7) under a nighttime ionosphere. Figure 19 makes it evident that spectral density from lightning is a complicated function of the apex radius, month, and local time as different land masses experience different meteorological and ionospheric conditions.

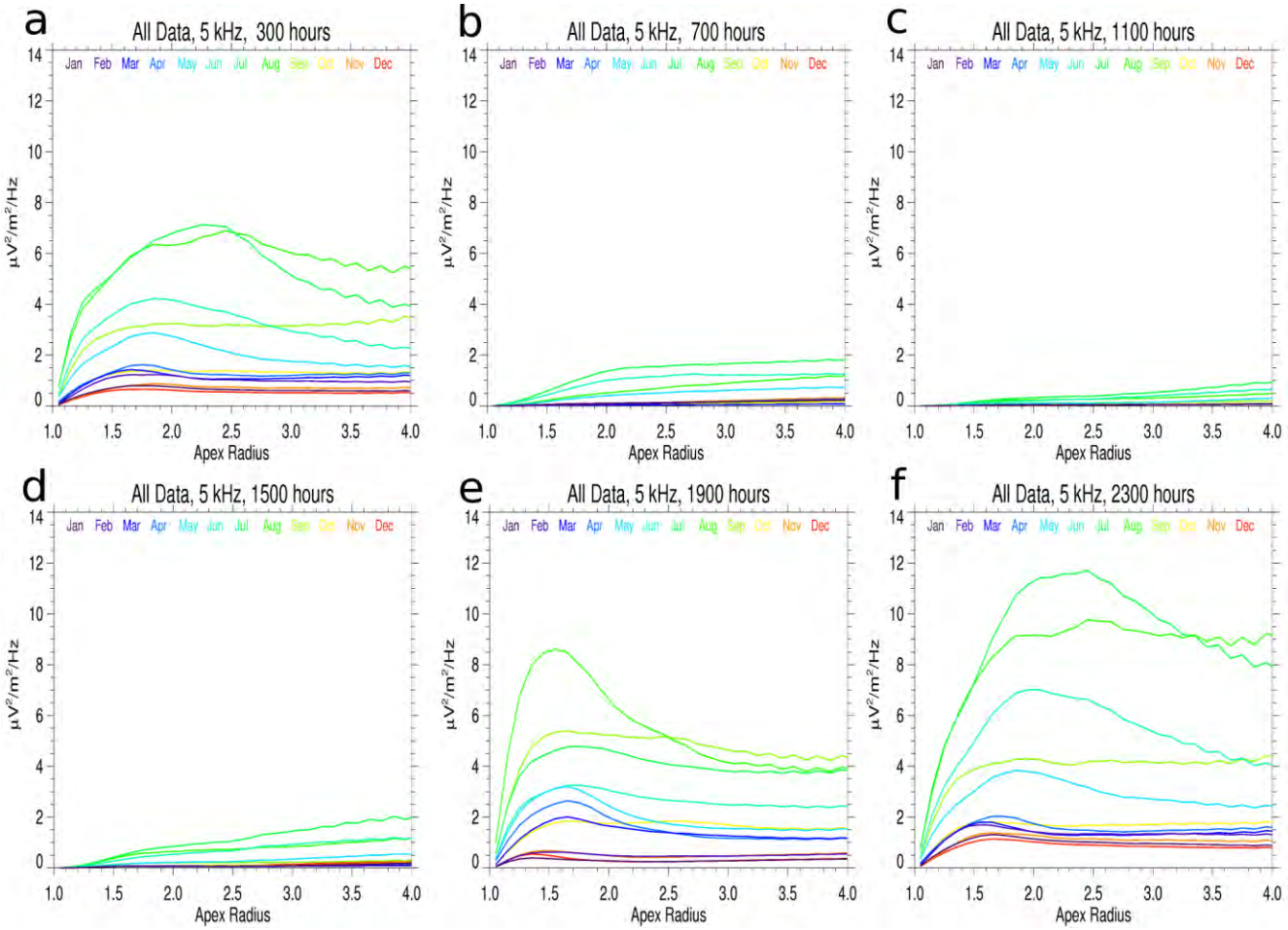

Figure 19. Spectral Density of the Scaled Climatology vs. Apex Radius

5. CONCLUSIONS

Starting from OTD/LIS lightning data representing 1995 – 2005, we have constructed a climatology of VLF spectral density from lightning at LEO. Key assumptions include: 1) a linear relationship between optical flash rate and VLF power flux; 2) VLF attenuation goes as the inverse distance in the earth-ionosphere waveguide (includes waveguide attenuation and sferic-whistler coupling); 3) transionospheric attenuation can be reasonably represented by the Helliwell curves; 4) 0+ whistler energy travels along field lines and shows up in the conjugate hemisphere without attenuation; and 5) the 5 years of DEMETER survey data reasonably represents the spectral density in LEO. Values are available for each month of the year and every two hours of local time on a 1°x1° spatial grid. The so constructed climatology shows complicated variation as a function of time and space.

This climatology represents a baseline treatment and there are some obvious improvements that could be tested and implemented. In addition it should be kept in mind that the observations to which this model is tied were mostly taken during the occurrence of an extreme solar minimum. There are parameters which could affect observed spectral power densities and which would also be affected by solar minimum conditions; such as the phase space density of energetic electrons

throughout the inner magnetosphere, and the location of the plasmapause. We now provide a brief summary of the models used for each organizational area of the framework including weaknesses and potential for improvement.

5.1 Terrestrial VLF Source Model

The Terrestrial VLF source model sprang from a combination of widely available LIS/OTD flash rate data sets provided by the Global Hydrology and Climate Center's Lightning Team. This same archive also contains time series data which could be used to infer the year to year spatial and temporal variations associated with the averages. Conversion to power flux was done via the assumption that flash rate is directly proportional to VLF power emitted. Spectral density was then derived by assuming an average spectral content per flash. The primary drawback of this procedure is that each flash in every storm is considered equivalent. It would be better to use a data set that included information about the distribution of power among strokes spatially, temporally, and even spectrally. Ground based lightning networks are currently operating which give global information on the spatial and temporal variation of VLF power, but they are still mostly in the research and development phase. These same networks can give spectral information as a function of distance from the strike. It would be of interest to use data from such networks to at least test the assumptions listed above.

5.2 Earth-Ionosphere Waveguide Propagation Model

The Earth-Ionosphere waveguide propagation model employed here is the simplest form, an inverse square law. Within line of sight viewing of the lightning strike from the bottom of the ionosphere this is likely a good approximation. Simple geometry tells us that from an altitude of 100 km the line of sight viewing is approximately $\cos^{-1}(6380/6480) = 10°$ or about 1000 km. This is very similar to the maximum distance for sferic to whistler conversion estimated from in situ rocket and satellite observations [32, 33, 51]. The main drawback to this approach is that there is no frequency dependent attenuation. It is likely that our approach underestimates attenuation at intermediate distances for frequencies below about 5 kHz and overestimates it above (see the mode theory discussion in Section 6 and [56]) but some of this effect is mitigated by the much larger ionospheric absorption at higher frequencies and the increasing reflection coefficient with increasing wave obliquity with respect to the lower ionospheric boundary. We most likely underestimate attenuation at long distances for all frequencies.

Short of a full waveguide mode treatment of the propagation it should be possible to transition from inverse square attenuation to a frequency dependent dB/Mm model at a distance near 1000 km. Different values should be used for day and night due the large difference in the lower ionospheric boundary altitude seen by VLF radiation. It is also probably true that the sferic to whistler conversion becomes less efficient at large distances as the wave vector becomes mostly horizontal to the earth's surface. Finally, there should be a geomagnetic intensity and dip angle dependence. These effects could be incorporated with a spatial dependence to the dB/Mm treatment. Spectrally dependent waveguide transport may be responsible for the fact that the overall spectral peak appears near 4 kHz. The peak might be expected at a lower frequency based on the incipient sferic spectrum and the steep rise in absorption as frequency decreases. An ameliorating factor might be the smaller attenuation experienced by higher frequencies in the waveguide. In addition there is very strong absorption below about 2 kHz due to the so called

cutoff frequency of the earth-ionosphere waveguide, e.g. [62]. This cutoff effect could drive the minimum seen at 1.6 kHz in Figure 9a which shows the seasonality of lightning. The other minimum below 1 kHz is most likely related to the proton cyclotron frequency in the ionosphere below which whistlers are said not to propagate. The proton cyclotron frequency is proportional to the magnitude of the magnetic field and so varies spatially, but is typically around 600 Hz in regions of interest. Neither of these effects are currently being treated and so power at frequencies below 2 kHz is probably overestimated in our climatology.

5.3 Trans-Ionospheric Attenuation Model

The Trans-Ionospheric attenuation model employed here originates in work by Helliwell [40]. In that work two simplified electron profiles in the ionosphere were assumed, one for daytime and another for nighttime conditions. The calculation proceeded in two parts one for the lower ionosphere (60 – 200 km) where electron neutral collisions dominate and the second for the F region (200 – 1500 km) where Coulomb interactions between electrons and ions dominate. A single vertical profile for each of total collisions and Coulomb collisions was employed. Absorption was calculated for vertically incident waves along the wave normal direction using a refractive index representing the Quasi-Longitudinal (QL) approximation. As previously discussed the major deficiency is the lack of known systematic variation in ionospheric profiles. The calculation is represented in some detail in [40] and was recently reproduced omitting the QL assumption, and then again with a full wave code [60], which showed the overall validity of the Helliwell approach. When compared to average ionospheric conditions calculated from the IRI the major difference was due to a sharper cutoff in electron densities below 80 km seen in the IRI nighttime profile, this difference lead to somewhat lower absorption. It would certainly be of interest to use IRI based ionospheric profiles, of whatever fidelity is computationally feasible. In leu of performing the large number of full wave calculations necessary to cover the range of dimensions addressed here (longitude, latitude, time of day, frequency = 360x120x12x205) it might be expeditious to use the calculation technique exactly as outlined by Helliwell, but with time and space electron profiles from the IRI; especially in light of the close agreement between it and the full wave calculation shown in [60] (Figure 2 of that work) when identical input parameters are utilized.

5.4 Magnetospheric Propagation Model

The Magnetospheric propagation model employed here is pure ducted. That is, we assume field aligned propagation only, while in-situ magnetospheric observations indicate that most whistlers are likely nonducted, e.g. [63]. It is known that whistler waves propagating in non-ducted mode through the ionosphere maintain vertical wave normal directions due to the strong gradient in electron density; but their group velocity direction is not vertical in this region due to the influence of the geomagnetic field. We have modeled transport through the ionosphere up to LEO as ducted (field aligned) propagation while ducts are thought to remain coherent only down to 1000 km or so. Thus transport of 0+ whistler up to LEO altitudes should likely be non-ducted and arrive somewhere between radial and field aligned with a frequency dependent component. This picture is borne out by observational studies as previously described [54]. Given the fidelity of this initial study such a correction is not expected to be important, but could be simply implemented in the future.

DEMETER observations show large amounts of power with the spatial/temporal character of lightning at and below 5 kHz in regions where there is very little lightning activity, but where there is activity in the conjugate region. Non-ducted transport calculations at these frequencies indicate that such waves should undergo MR above DEMETER orbit altitudes. So it seems that ducted transport is important. This may include one sided ducting associated with one way plasma gradients such as the plasmapause [64] as well as the traditional field aligned perturbations. DEMETER observations also show LHR hiss in these same conjugate regions, which is undoubtedly associated with non-ducted waves. So, non-ducted transport is also important. The LHR associated waves could be high enough frequency to not have undergone MR before reaching LEO. The one axis electric field measurements considered here cannot distinguish between longitudinal and oblique propagation. There is some suggestion in the literature that the chance of ducted propagation has a latitudinal dependence, with predominantly non-ducted transport being available below L=1.6 or so [65, 66]. Comparing the model and observations for July nighttime at 5 kHz shown in Figure 18 we see that the low latitude leg of the North American continent (Mexico – Panama) shows up in the conjugate model intensities but not in the observations; consistent with this hypothesis. It seems likely that the LHR hiss observed in conjugate regions has its origins in non-ducted waves originating from lower latitudes, while the spectral density around 5 kHz has its origins in ducted waves from the conjugate field line location.

In practice the assumption of ducted transport simplifies the calculations greatly. This is because there is no spatially dependent frequency dispersion. While in non-ducted transport the wave embarks on a whole new spatial trajectory at each MR until it settles at an apex radius characteristic of its frequency (which has an equatorial LHR approximately equal to the wave frequency according to [67]). Thus for ducted transport a given location in the apex coordinate system only has contributions from other locations along that field line, but for nonducted transport a given location can have contributions from a large number of other locations. In this initial treatment, and where we are only trying to represent spectral density at LEO, we have found a pure ducted treatment expedient and sufficient. However, in order to fill the inner magnetosphere with waves from lightning it would be necessary to make some assumption about at least the relative occurrence of ducted and non-ducted waves. As in Able and Thorne [1998], where it was assumed that each accounted for roughly the same amount of spectral density and the same relative occurrence. While such an estimate is beyond the scope of this initial investigation we will note that the overall spatial temporal spectral information within the DEMETER data set could give some insight in to the relative proportions for reasons already outlined above.

The ultimate purpose of this investigation was to give estimates of the VLF power in LEO at a two hour cadence for each month of the year. However, in order to characterize the sources and sinks of energetic electrons in the radiation belts the spectral power densities derived here must be used as input to a calculation of pitch angle diffusion coefficients which could then be used to estimate particle lifetimes. Although we have used only ducted transport calculations here, in practice these spectral power densities could be used as input to either ducted or nonducted transport calculations since the scalings and correlations are based on total power. The climatologies reported here represent a step forward from the single numbers used in Able and

Thorne [10], or even the L and AE dependent values derived by Meredith et al. [23]. Work on converting these spectral power density estimates into radiation belt particle lifetimes is ongoing.

Acknowledgments. The LIS/OTD HRMC_COM_FR (monthly) and LRADC_COM_SMFR2 climatology data were produced by the LIS/OTD Science Team (Principal Investigator, Hugh J. Christian, NASA/MSFC) and were obtained from the Global Hydrology Research Center (GHRC) (http://ghrc.msfc.nasa.gov/). The DEMETER observations were provided by the Stanford VLF group and the DEMETER satellite team. The author would like to thank the Stanford VLF team (particularly N. G. Lehtinen and R. K. Said) and the AFRL Wave-Particle Interactions team (particularly M. J. Starks) for useful discussions.

References

[1] Thorne, R. M. (1977), Energetic radiation belt electron precipitation: A natural depletion mechanism for stratospheric ozone, *Science*, 21, 287–289.
[2] Rozanov, E., L. Callis, M. Schlesinger, F. Yang, N. Andronova, and V. Zubov (2005), Atmospheric response to NOy source due to energetic electron precipitation, *Geophys. Res. Lett.*, 32, L14811, doi:10.1029/2005GL023041.
[3] Bullough, K., A.R.L Tatnall, and M. Derby (1976), Man-made e.l.f./v.l.f. Emissions and the radiation belts, *Nature*, 250, 401-403, doi:10.1038/260401a0.
[4] Parrot, M. (1990), World map of ELF/VLF emissions as observed by a low-orbiting satellite, *Ann. Geophys.*, 8, 135–145.
[5] André, R., F. Lefeuvre, F. Simonet, and U. S. Inan (2002), A first approach to model the low-frequency wave activity in the plasmasphere, *Ann. Geophys.*, 20, 981–996.
[6] Baker D. N., S. G. Kanekal, R. B. Horne, N. P. Meredith, and S. A. Glauert (2007), Low-altitude measurements of 2–6 MeV electron trapping lifetimes at $1.5 \leq L \leq 2.5$, *Geophys. Res. Lett.*, 34, L20110, doi:10.1029/2007GL031007.
[7] Meredith, M. P., R. B. Horne, S. A. Glauert, D. N. Baker, S. G. Kanekal, and J. M. Albert (2009), Relativistic electron loss timescales in the slot region, *J. Gophys. Res.*, 114, A03222, doi:10.1029/2008JA013889.
[8] Lyons, L. R., and R. M. Thorne, Equilibrium Structure of Radiation Belt Electrons (1973), *J. Geophys. Res.*, 78, 2142.
[9] Cornwall J. M. (1965), Cyclotron Instabilities and Electromagnetic Emissions in the Ultra Low Frequency and Very Low Frequency Ranges, *J. Geophys. Res.*, 70(1), 61-69.
[10] Abel, B., and R. M. Thorne (1998a), Electron scattering loss in Earth's inner magnetosphere: 1. Dominant physical processes, *J. Geophys. Res.*, 103(A2), 2385–2396, doi:10.1029/97JA02919.
[11] Abel, B., and R. M. Thorne (1998b), Electron scattering loss in Earth's inner magnetosphere 2. Sensitivity to model parameters, *J. Geophys. Res.*, 103, A2, 2397-2407, doi:10.1029/97JA02920.
[12] Abel, B., and R. M. Thorne (1999), Correction to "Electron scattering loss in Earth's inner magnetosphere: 1. Dominant physical processes" and "Electron scattering loss in Earth's inner magnetosphere: 2. Sensitivity to model parameters" by Bob Abel and Richard M. Thorne, *J. Geophys. Res.*, 104, 4627–4628, doi:10.1029/1998JA900121.
[13] Thorne R. M., E. J. Smith, R. K. Burton, and R. E. Holzer (1973), Plasmaspheric Hiss, *J. Geophys. Res.*, 78, 10, 1581-1596.
[14] Tsurutani, B. R., E. J. Smith, and R. M. Thorne (1975), Electromagnetic Hiss and Relativistic Electron Losses in the Inner Zone, *J. Geophys. Res.*, 80(4), 600-607.
[15] Burgess, W. C., and U. S. Inan (1993), The Role of Ducted Whistlers in the Precipitation Loss and Equilibrium Flux of Radiation Belt Electrons, *J. Geophys. Res.*, 98, A9, 15643-15665.
[16] Draganov, A. B., U. S. Inan, V. S. Sonwalkar, and T. F. Bell (1993), Whistlers and Plasmaspheric Hiss: Wave directions and Three-Dimensional Propagation, *J. Geophys. Res.*, 98, A7, 11401-11410.
[17] Inan, U. S., H. C. Chang, and R. A. Helliwell (1984), Electron precipitation zones around major ground-based VLF signal sources, *J. Geophys. Res.*, 89(A5), 2891– 2906, doi:10.1029/JA089iA05p02891.

[18] Starks, M. J., R. A. Quinn, G. P. Ginet, J. M. Albert, G. S. Sales, B. W. Reinisch, and P. Song (2008), Illumination of the plasmasphere by terrestrial very low frequency transmitters: Model validation, *J. Gophys. Res.*, 113, A09320, doi:10.1029/2008JA013112.
[19] Starks, M. J., T. F. Bell, R. A. Quinn, U. S. Inan, D. Piddyachiy, and M. Parrot (2009), Modeling of Doppler-shifted terrestrial VLF transmitter signals observed by DEMETER, *Geophys. Res. Lett.*, 36, L12103, doi:10.1029/2009GL038511.
[20] Storey, L. R. O. (1953), An investigation of whistling atmospherics, *Philos. Trans. R. Soc. London*, Ser. A, 246, 113– 141.
[21] Kimura, I. (1966), Effects of ions on whistler-mode ray tracing, Radio Sci., 1(3), 269– 283.
[22] Smith, R. L., J. J. Angerami (1968), Magnetospheric Properties Deduced from OGO 1 Observations of Ducted and Nonducted Whistlers, *J. Geophys. Res.*, 73(1), 1-20.
[23] Meredith, M. P., R. B. Horne, S. A. Glauert, and R. R. Anderson (2007), Slot region electron loss timescales due to plasmaspheric hiss and lightning-generated whistlers, *J. Gophys. Res.*, 112, A08214, doi:10.1029/2007JA012413.
[24] Lauben, D. S., U. S. Inan and T. F. Bell (2001), Precipitation of radiation belt electrons induced by obliquely propagating lightning-generated whistlers, *J. Geophys. Res.*, 106(A12), 29745-29770.
[25] Rycroft, M. J. (1973), ENHANCED ELECTRON INTENSITIES AT 100 km ALTITUDE AND A WHISTLER PROPAGATING THROUGH THE PLASMASPHERE, *Planet. Space. Sci.*, 21, 239-251.
[26] Voss, H. D., W. L. Imhof, J. Mobilia, E. E. Gaines, M. Walt, U.S. Inan, R. A. Helliwell, D. L. Carpenter, J. P. Katsufrakisa, and H. C. Chang (1984), Lightning-induced electron precipitation, *Nature*, 312, 740.
[27] Helliwell, R. A., J. P. Katsufrakis, and M. L. Trimpi (1973), Whistler-Induced Amplitude Perturbation in VLF Propagation, *J. Geophys. Res.*, 78(22), 4679-4688.
[28] Voss, H. D., M. Walt, W. L. Imhof, J. Mobilia, U.S. Inan (1989), Satellite observations of lightning-induced electron precipitation, *J. Geophys. Res.*, 103, A6, 11725-11744.
[29] Bortnik, J., U. S. Inan, and T. F. Bell (2003), Energy distribution and lifetime of magnetospherically reflecting whistlers in the plasmasphere, *J. Geophys. Res.*, 108(A5), 1199, doi:10.1029/2002JA009316.
[30] Inan, U. S., D. Piddyachiy, W. B. Peter, J. A. Sauvaud, and M. Parrot (2007), DEMETER satellite observations of lightning-induced electron precipitation, *Geophys. Res. Lett.*, 34, L07103, doi:10.1029/2006GL029238.
[31] Gemelos, E. S., U. S. Inan, M. Walt, M. Parrot, and J. A. Sauvaud (2009), Seasonal dependence of energetic electron precipitation: Evidence for a global role of lightning, *Geophys. Res. Lett.*, 36, L21107, doi:10.1029/2009GL040396.
[32] Holzworth, R. H., R. M. Winglee, B. H. Barnum, Y. Li, and M. C. Kelley (1999), Lightning whistler waves in the high-latitude magnetosphere, *J. Geophys. Res.*, 104, 17,369–17,378, doi:10.1029/1999JA900160.
[33] Chum, J., Jiříček, F., Santolik, O., Parrot, M., Diendorfer, G., and Fiser, J. (2006), Assigning the causative lightning to the whistlers observed on satellites, *Ann. Geophys.*, 24, 2921–2929.
[34] Said, R. K., U. S. Inan, and K. L. Cummins (2010), Long-range lightning geolocation using a VLF radio atmospheric waveform bank, *J. Geophys. Res.*, 115, D23108, doi:10.1029/2010JD013863.

[35] Sato, M., Y. Takahashi, A. Yoshida, and T. Adachi (2008), Global distribution of intense lightning discharges and their seasonal variations, *J. Phys. D.: Appl. Phys.*, 41, 234011-234020.
[36] Collier, A. B., S. Bremner, J. Lichtenberger, J. R. Downs, C. J. Rodger, P. Steinbach, and G. McDowell (2010), Global lightning distribution and whistlers observed at Dunedin New Zealand, *Ann. Geophys.*, 28, 499-513.
[37] VanZandt, T. E., W. L. Clark, and J. M. Warnock (1972), Magnetic Apex Coordinates: A Magnetic Coordinate System for the Ionospheric F2 Layer, *J. Geophys. Res.*, 77(13), 2406-2411.
[38] McIlwain, C. E. (1961), Coordinates for Mapping the Distribution of Magnetically Trapped Particles, *J. Geophys. Res.*, 66(11), 3681-3691.
[39] Berthelier, J. J., et al. (2006), ICE, the electric field experiment on DEMETER, *Planet. Space Sci.*, 54, 456– 471, doi:10.1016/j.pss.2005.10.016.
[40] Helliwell, R. A. (1965), Whistlers and Related Ionospheric Phenomena, Stanford Univ. Press, Stanford, Calif.
[41] Christian, H. J., et al. (2003), Global frequency and distribution of lightning as observed from space by the optical transient detector, *J. Geophys. Res.*, 108(D1), 4005, doi:10.1029/2002JD002347.
[42] Lay, E. H., A. R. Jacobson, R. H. Holzworth, C. J. Rodger, and R. L. Dowden (2007), Local time variation in land/ocean lightning flash density as measured by the World Wide Lightning Location Network, *J. Geophys. Res.*, 112, D13111, doi:10.1029/2006JD007944.
[43] Mach, D. M., R. J. Blakeslee, and M. G. Bateman (2011), Global electric circuit implications of combined aircraft storm electric current measurements and satellite-based diurnal lightning statistics, *J. Geophys. Res.*, 116, D05201, doi:10.1029/2010JD014462.
[44] Abarca, S. F., K. L. Corbosiero, and T. J. Galarneau Jr. (2010), An evaluation of the Worldwide Lightning Location Network (WWLLN) using the National Lightning Detection Network (NLDN) as ground truth, *J. Geophys. Res.*, 115, D18206, doi:10.1029/2009JD013411.
[45] Parrot, M., J. A. Sauvaud, J. J. Berthelier, and J. P. Lebreton (2007), First in-situ observations of strong ionospheric perturbations generated by a powerful VLF ground-based transmitter, *Geophys. Res. Lett.*, 34, L11111, doi:10.1029/2007GL029368.
[46] Brice N. M., and R. L. Smith (1965), Lower hybrid resonance emissions, *J. Geophys. Res.*, 70, 71–80.
[47] Bell, T. F., H. D. Ngo (1990), Electrostatic Lower Hybrid Waves Excited by Electromagnetic Whistler Mode Waves Scattering From Planar Magnetic-Field-Aligned Plasma Density Irregularities, *J. Geophys. Res.*, 95, 149-172.
[48] Shklyar, D. R., and H. Washimi (1994), Lower hybrid resonance wave excitation by whistlers in the magnetospheric plasma, *J. Geophys. Res.*, 99(A12), 23695-23704.
[49] Shklyar, D. R., M. Parrot, J. Chum, O. Santolik, and E. E. Titova (2010), On the origin of lower- and upper-frequency cutoffs on wedge-like spectrograms observed by DEMETER in the midlatitude ionosphere, *J. Geophys. Res.*, 115, A05203, doi:10.1029/2009JA014672.
[50] Němec, F., O. Santolík, M. Parrot, and C. J. Rodger (2010), Relationship between median intensities of electromagnetic emissions in the VLF range and lightning activity, *J. Geophys. Res.*, 115, A08315, doi:10.1029/2010JA015296.
[51] Santolík, O., M. Parrot, U. S. Inan, D. Burešová, D. A. Gurnett, and J. Chum (2009), Propagation of unducted whistlers from their source lightning: A case study, *J. Geophys. Res.*, 114, A03212, doi:10.1029/2008JA013776.
[52] Füllekrug, M., C. Price, Y. Yair, and E. R. Williams (2002), Intense oceanic lightning, *Ann. Geophys.*, 20, 133-137.

[53] Thomas, J. N., B. H. Barnum, E. Lay, R. H. Holzworth, M. Cho, and M. C. Kelley (2008), Lightning-driven electric fields measured in the lower ionosphere: Implications for transient luminous events, *J. Geophys. Res.*, 113, A12306, doi:10.1029/2008JA013567.
[54] Fiser, J., J. Chum, G. Diendorfer, M. Parrot, and O. Santolík (2010), Whistler intensities above thunderstorms, *Ann. Geophys.*, 28, 37–46.
[55] Ferencz, O. E., C. Ferencz, P. Steinbach, J. Lichtenberger, D. Hamar, M. Parrot, F. Lefeuvre, and J.-J. Berthelier (2007), The effect of subionospheric propagation on whistlers recorded by the DEMETER satellite - observation and modelling, *Ann. Geophys.*, 25, 1103–1112.
[56] Wait, J. R. (1957), The Attenuation vs Frequency Characteristics of VLF Radio Waves, *P. IRE*, June, 768-771.
[57] Le Vine, D. M. (1986), Review of Measurements of the RF Spectrum of Radiation from Lightning, NASA Technical Memorandum 87788.
[58] Dowden R. L., J. B. Brundell, and C. J. Rodger (2002), VLF lightning location by time of group arrival (TOGA) at multiple sites, *J. Atmos. Sol.-Terr. Phys.*, 64, 817-830.
[59] Watt, J. R. (1967), VLF Radio Engineering, Pergamon Press, London, Great Britain.
[60] Tao, X., J. Bortnik, and M. Friedrich (2010), Variance of transionospheric VLF wave power absorption, *J. Geophys. Res.*, 115, A07303, doi:10.1029/2009JA015115.
[61] Lehtinen, N. G., Inan U. S. (2009), Full-wave modeling of transionospheric propagation of VLF waves, *Geophys. Res. Lett.*, 36, L03104, doi:10.1029/2008GL036535.
[62] Cummer, S. A. (2000), Modeling electromagnetic propagation in the Earthionosphere waveguide, *IEEE T. Anten. Propag.*, 48(9), 1420–1429.
[63] Hughes, A. R. W., W. K. A. Rice (1997), Satellite study of low latitude electron and proton whistlers, *J. Atmos. Sol.-Terr. Phys.*, 59(10), 1217-1222.
[64] Inan, U. S., and T. F. Bell (1977), The plasmapause as a VLF waveguide, *J. Geophys. Res.*, 82(19), 2819– 2827, doi:10.1029/JA082i019p02819.
[65] Clilverd, M. A., C. J. Rodger, R. Gamble, N. P. Meredith, M. Parrot, J.-J. Berthelier, and N. R. Thomson (2008), Ground-based transmitter signals observed from space: Ducted or nonducted?, *J. Geophys. Res.*, 113, A04211, doi:10.1029/2007JA012602.
[66] Rodger, C. J., B. R. Carson, S. A. Cummer, R. J. Gamble, M. A. Clilverd, J. C. Green, J.-A. Sauvaud, M. Parrot, and J.-J. Berthelier (2010), Contrasting the efficiency of radiation belt losses caused by ducted and nonducted whistler-mode waves from ground-based transmitters, *J. Geophys. Res.*, 115, A12208, doi:10.1029/2010JA015880.
[67] Bortnik, J., U. S. Inan, and T. F. Bell (2002), L dependence of energetic electron precipitation driven by magnetospherically reflecting whistler waves, *J. Geophys. Res.*, 107(A8), 1150, doi:10.1029/2001JA000303.

DISTRIBUTION LIST

DTIC/OCP
8725 John J. Kingman Rd, Suite 0944
Ft Belvoir, VA 22060-6218 1 cy

AFRL/RVIL
Kirtland AFB, NM 87117-5776 2 cys

Official Record Copy
AFRL/RVBXT/Christopher Sillence 1 cy

This page is intentionally left blank.